FHOD-1 is the only formin in *Caenorhabditis elegans* that promotes striated muscle growth and Z-line organization in a cell autonomous manner

Sumana Sundaramurthy[1], **SarahBeth Votra**[1], **Arianna Laszlo**[1], **Tim Davies**[2,3], **David Pruyne**[1,4]

[1]Department of Cell and Developmental Biology, State University of New York Upstate Medical University, Syracuse, NY

[2]Department of Pathology and Cell Biology, Columbia University, New York, NY

[3]Present address: Department of Biosciences, Durham University, Durham, UK

Abstract

The striated body wall muscles of *Caenorhabditis elegans* are a simple model for sarcomere assembly. Previously, we observed deletion mutants for two formin genes, *fhod-1* and *cyk-1,* develop thin muscles with abnormal dense bodies (the sarcomere Z-line analogs). However, this work left in question whether these formins work in a muscle cell autonomous manner, particularly since *cyk-1( )* deletion has pleiotropic effects on development. Using a fast acting temperature-sensitive *cyk-1(ts)* mutant, we show here that neither post-embryonic loss nor acute loss of CYK-1 during embryonic sarcomerogenesis cause lasting muscle defects. Furthermore, mosaic expression of CYK-1 in *cyk-1( )* mutants is unable to rescue muscle defects in a cell autonomous manner, suggesting muscle phenotypes caused by *cyk-1( )* are likely indirect. Conversely, mosaic expression of FHOD-1 in *fhod-1( )* mutants promotes muscle cell growth and proper dense body organization in a muscle cell autonomous manner. As we observe no effect of loss of any other formin on muscle development, we conclude FHOD-1 is the only worm formin that directly promotes striated muscle development, and the effects on formin loss in *C. elegans* are surprisingly modest compared to other systems.

Keywords

striated muscle; formin; dense bodies; sarcomere Z-line; *Caenorhabditis elegans*

Introduction

Striated muscles, found widely across the animal kingdom (Clark, McElhinny, Beckerle, & Gregorio, 2002), are so-called due to the appearance of striations composed of regularly repeating contractile units, called sarcomeres. Each sarcomere is bordered by Z-lines that anchor actin-based thin filaments, while myosin-based thick filaments interdigitate between

---

[4]Corresponding author.

thin filaments and are anchored at the M-line at the sarcomere center. Besides these major cytoskeletal components, the contractile lattice is made up of additional proteins that help maintain structure and function (Henderson, Gomez, Novak, Mi-Mi, & Gregorio, 2017).

Evidence from multiple model systems demonstrates formins contribute to the assembly of sarcomeres. Formins are stimulators of actin assembly that function largely through two conserved Formin Homology (FH) domains, the FH1 and FH2. When dimerized, FH2 domains nucleate actin filaments from monomers, and remain associated with the growing barbed-end of the filament, protecting the end from inhibitors of elongation, like capping proteins (Pruyne et al., 2002; Sagot, Rodal, Moseley, Goode, & Pellman, 2002; Pring, Evangelista, Boone, Yang, & Zigmond, 2003; Kovar & Pollard, 2004; Moseley et al., 2004). The proline-rich FH1 domain recruits profilin bound to actin monomers to allow monomer addition to the barbed ends (Chang, Drubin, & Nurse, 1997; Evangelista et al., 1997; Imamura et al., 1997; Romero et al., 2004; Kovar, Harris, Mahaffy, Higgs, & Pollard, 2006).

Based on sequence homology, animal formins are grouped into nine families (Higgs & Peterson, 2005; Pruyne, 2016). One member of the FHOD-family, FHOD3, is the best-studied vertebrate formin for its effects on muscle development. Variants of the *fhod3* gene have been associated with occurrence of hypertrophic and dilated cardiomyopathies in humans (Arimura et al., 2013; Wooten et al., 2013; Hayashi et al., 2018; Ochoa et al., 2018), while its knock out in mice results in lethality at embryonic day 11.5 due to cardiac insufficiency, with failure to form mature myofibrils in cardiac muscle (Kan-O et al., 2012). This crucial role for FHOD3 depends on its ability to interact with actin (Fujimoto et al., 2016). Studies with human induced pluripotent stem cell-derived cardiomyocytes and cultured rat cardiomyocytes confirm FHOD3 regulates myofibrillogenesis (Taniguchi et al., 2009; Iskratsch et al., 2010; Fenix et al., 2018). Studies in *Drosophila* indirect flight muscles (IFMs) have shown complete absence of fly FHOD-family formin FHOS abolishes sarcomere organization, while early knockdown yields thin, irregular myofibrils with dispersed and rudimentary Z-discs, and late knockdown prevents thin filament elongation or new thin filament incorporation (Shwartz, Dhanyasi, Schejter, & Shilo, 2016).

DAAM-family formins have also been implicated in muscle development. In *Drosophila* IFMs, and to a lesser extent heart and larval body wall muscle, absence of DAAM leads to thin myofibrils with reduced F-actin and thick filament content, and abnormal Z-discs and M-lines (Molnár et al., 2014). In mice, conditional DAAM1 knock out led to non-compaction cardiomyopathy, while simultaneous knock out of DAAM1 and DAAM2 caused stronger myopathy, severely reduced cardiac function, and disrupted sarcomere structure (Ajima et al., 2015). An RNA interference (RNAi)-based study of cultured neonatal mouse cardiomyocytes confirmed the importance of DAAM1 for myofibril organization, and also implicated FMNL- and DIAPH-family formins FMNL1, FMNL2, and DIAPH3 (Rosado et al., 2014). While these studies suggest formins promote sarcomere organization, it is not clear what roles they play.

Our work with the simple model nematode *Caenorhabditis elegans* also implicates formins in promoting sarcomere formation in striated muscle. The worm has two pairs of body wall muscles (BWMs) that extend the length of the animal in dorsal and ventral positions. Each

BWM cell consists of a cell body overlying a spindle-shaped myofilament lattice that is adherent to a basal lamina. Distinct from cross-striated vertebrate or fly muscle, BWM is obliquely striated with striations oriented at a 6° angle with respect to the longitudinal axis of the cell. The majority of thin filaments are anchored at dense bodies (DBs), which are analogous to vertebrate Z-discs, whereas thick filaments are attached to M-lines (Moerman & Williams, 2006; Gieseler, Quadota, & Benian, 2017). In BWM, all DBs and M-lines are also attached to the plasma membrane, and based on protein composition, DBs also resemble costameres and focal adhesions (Lecroisey, Ségalat, & Gieseler, 2007).

Many sarcomeric proteins and interactions are conserved between *C. elegans* BWM and mammalian striated muscle (Benian & Epstein, 2011). But unlike mammals, where fifteen genes represent seven of the nine animal formin families, *C. elegans* has only six formin genes (*fhod-1, cyk-1, daam-1, frl-1, exc-6* and *inft-2*) representing five families (Pruyne, 2016). Due to this simplicity, *C. elegans* BWM serves as a good model to study roles of formins in the development and function of striated muscle.

We previously characterized BWM defects in mutants for five worm formin genes (Mi-Mi, Votra, Kemphues, Bretscher, & Pruyne, 2012; Mi-Mi & Pruyne, 2015). Among these, only loss of FHOD-family FHOD-1 and DIAPH-family CYK-1 resulted in BWM defects. Based on the tendency of formins to promote assembly of long, unbranched actin filaments *in vitro*, an attractive model was that FHOD-1 and CYK-1 initiate assembly of the actin-based thin filaments, with the prediction that absence of both formins should prevent thin filament formation. The deletion alleles *fhod-1(tm2363)* and *cyk-1(ok2300)*, referred to hereafter as *cyk-1( )* and *fhod-1( )*, eliminate part or all of their respective FH2 domains, making them putative nulls for formin-mediated actin assembly. Either *fhod-1( )* or *cyk-1( )* individually results in thin BWM cells with fewer striations per cell, while mutants for both formin genes have even thinner BWM cells, suggesting overlapping roles in muscle (Mi-Mi et al., 2012). However, BWM in those double mutants still have thin filaments organized in sarcomeres (Mi-Mi & Pruyne, 2015), inconsistent with our initial prediction.

A complication to that analysis was that CYK-1 is also essential for cytokinesis during embryonic development (Swan et al., 1998). To circumvent this requirement, *cyk-1( )* was maintained in a heterozygous background. Homozygous *cyk-1( )* mutants that arose as one quarter of the progeny from *cyk-1( )/+* parents completed embryogenesis due to inheritance of maternally-provided CYK-1 protein/mRNA (Mi-Mi et al., 2012). This also left open the possibility maternally inherited CYK-1 supported some sarcomere assembly. Another complication was *cyk-1( )* has pleiotropic effects on development (Mi-Mi et al., 2012), allowing the possibility that muscle effects were secondary to other primary defects. Elimination of CYK-1 by RNAi yielded the same phenotypes as *cyk-1( )* (Mi-Mi et al., 2012), but slow onset of RNAi also allowed for residual CYK-1 in developing muscle, and pleiotropic effects again complicated interpretation.

Recent isolation of a fast acting temperature-sensitive *cyk-1* allele (Davies et al., 2014), and the generation here of strains with mosaic expression of wild-type formin, have allowed us to re-examine this question. We find here CYK-1 plays a non-cell autonomous role in promoting muscle growth, likely during early embryogenesis, leaving FHOD-1 the only

formin to play a cell autonomous role in BWM development. We also observe that in contrast to vertebrate and insect muscle, worm BWM is strikingly resilient to loss of endogenous formin.

Results

Post-embryonic CYK-1 loss leads to minimal BWM developmental defects.

The vast majority of BWM growth and sarcomere assembly occurs after embryogenesis, when worms grow ~200-fold in size from L1 stage larvae to adults. If formins were required for sarcomere assembly, we would expect their absence to very significantly impact muscle growth during this period. To test the contribution of CYK-1 without the complications incurred by *cyk-1( )* or *cyk-1(RNAi)*, we utilized the fast acting temperature-sensitive allele *cyk-1(or596ts)*, whose product supports embryonic development at a permissive temperature of 16°C, but becomes inactive within 5 min after shift to 26°C (Davies et al., 2014). We combined *cyk-1(ts)* with *fhod-1( )* to allow complete elimination of CYK-1 and FHOD-1 function during post-embryonic development. Age synchronized L1 stage larvae of wild-type, *cyk-1(ts)*, *fhod-1( )*, or the combined *fhod-1( ); cyk-1(ts)* background, were shifted to either permissive or restrictive temperature and allowed to develop. Worms were collected every 12 hours and stained with fluorescently labeled phalloidin to visualize filamentous actin (F-actin) to track BWM growth. Prior to temperature shift, approximately 10% of the *cyk-1(ts)* and *fhod-1( )* single mutants and 20% of the *fhod-1( ); cyk-1(ts)* double mutants failed in body elongation during embryogenesis, an effect related to formin functions in the epidermis, as described previously for *fhod-1* and *cyk-1* (Vanneste, Pruyne, & Mains, 2013; Refai, Smit, Votra, Pruyne, & Mains, 2018). As these larvae died soon after hatching, they were excluded from analysis. For remaining animals, total body width (as a proxy for overall body size), BWM width, and individual BWM cell widths (based on F-actin stain) were measured (Figure 1, Figure S1).

At permissive temperature, *cyk-1(ts)* mutants grew normally, whereas at restrictive temperature, they laid no eggs and often developed protruding vulvas, phenotypes previously observed in *cyk-1( )* mutants (Mi-Mi et al., 2012). As expected, BWM widths of all strains increased at permissive temperature as the animals grew, but more slowly in *fhod-1( )* animals due to slower growth of individual muscle cells (Figure S1 A, B). In *cyk-1(ts)* mutants, we also observed narrower BWMs and narrower individual muscle cells compared to wild type at permissive temperatures, although this effect was less than for *fhod-1( )* animals (Figure S1 A, B), suggesting the *cyk-1(ts)* allele may be partially non-functional at 16°C. At the restrictive temperature, muscle cells in *fhod-1( )* mutants again grew slower than wild type, as expected (Figure 1 A–C). Surprisingly, BWM and muscle cells of *cyk-1(ts)* were only minimally reduced for growth compared to wild type, while those of *fhod-1( ); cyk-1(ts)* double mutants were similar to *fhod-1( )* mutants (Figure 1 A–C). These effects were much weaker than we had observed for *cyk-1( )* (Mi-Mi et al., 2012).

We considered formins might affect overall body growth, and that reduced BWM might simply reflect smaller body size. Indeed, absence of FHOD-1 very modestly reduces body growth, and *cyk-1( )* animals are significantly smaller than wild type (Mi-Mi et al., 2012; Refai et al., 2018). Thus, we measured the overall body widths of worms grown at 26°C

(Figure1 D, Figure S1 C), and determined the ratios of the BWM widths to total body. This average ratio was fairly constant for each strain throughout growth, and was similar between *cyk-1(ts)* and wild type (Figure 1 E). Ratios for *fhod-1( )* and *fhod-1( ); cyk-1(ts)* double mutants were also similar to each other, but proportionately smaller than wild type at all ages (Figure 1 E). To determine whether this relationship held for individual worms, as opposed to average results for a population, we plotted BWM and total body widths for individual animals grown at 26°C, and observed nearly identical linear relationships between muscle and body size for wild-type and *cyk-1(ts)* animals, while those for *fhod-1( )* and double mutants were different from wild type, but similar to each other (Figure 1 F). These data confirm absence of FHOD-1 disrupts BWM growth to a greater extent than overall growth, whereas the modest BWM growth defects of *cyk-1(ts)* animals might be a consequence of reduced overall body size.

Our previous work suggested three of the remaining four formins in *C. elegans* (EXC-6/ INFT-1, INFT-2, and FRL-1) make no obvious contribution to BWM development (Mi-Mi et al., 2012). We had also observed an FH2-targeting deletion of the formin gene *daam-1* caused no obvious synthetic defects in combination with *fhod-1( )* (Mi-Mi et al., 2012), but careful analysis was not performed due to a deletion of thirteen genes very tightly linked to *daam-1* that caused additional growth defects (Mangio, Votra, & Pruyne, 2015). Using CRISPR/Cas9-based genome editing, we generated a novel FH2-null *daam-1* allele, *ups39*. On inspecting BWM in age-synchronized adult *daam-1(ups39)* mutants and *fhod-1( )*; *daam-1(ups39)* double mutants, we observed no effect of absence of DAAM-1 in either background (Figure S2). Our current data suggest FHOD-1 might be the only formin that specifically supports BWM growth during post-embryonic development in *C. elegans*.

Constitutive absence of FHOD-1 or CYK-1, but not post-embryonic loss of CYK-1, disrupts dense body (DB) organization in adult BWM.

DBs serve as sarcomere Z-lines in BWM, and are structurally and compositionally similar to vertebrate focal adhesions and costameres (Lecroisey et al., 2007). The most prominent feature of these complex structures is an α-actinin (ATN-1)-rich portion that extends into the contractile lattice to anchor thin filaments (Gieseler et al., 2017). By transmission electron microscopy (TEM), DBs in wild-type BWM appear as distinct electron-dense finger-like protrusions, while in *fhod-1( )* mutants they appear as multiple thinner electron-dense strands (Mi-Mi & Pruyne, 2015). Correlating with this, immunostain for ATN-1 reveals DBs as discrete puncta in wild-type BWM, but appears partially dispersed in *fhod-1( )* mutants (Figure 2).

By TEM, *cyk-1( )* and *fhod-1( ); cyk-1( )* mutant BWMs have less to almost no electron-dense material at some locations where DBs are otherwise expected (Mi-Mi & Pruyne, 2015). Consistent with this, ATN-1 immunostain of adult *cyk-1( )* mutants and *fhod-1( )*; *cyk-1( )* double mutants revealed a variable staining. Some BWM regions showed prominent wild-type-appearing puncta in *cyk-1( )* mutants, or *fhod-1( )*-like dispersed structures in *cyk-1( ); fhod-1( )* double mutants (Figure 2, arrows), while other regions had no observable ATN-1-containing structures (arrowheads). Regions of absent staining were observed only in worms with *cyk-1( )* in their genetic background, and we still observed

diffuse background stain in these regions, suggesting this does not reflect failure of antibody penetration.

Because our results with *cyk-1(ts)* suggested postembryonic loss of CYK-1 does not affect BWM cell growth, we examined whether post-embryonic loss of CYK-1 had a similar lack of effect on DB morphology. L1 larvae were grown to adulthood at the restrictive temperature before immunostaining for ATN-1. In contrast to *cyk-1( )* mutants, DBs in *cyk-1(ts)* mutants consistently appeared wild-type, with no areas lacking ATN-1 stain (Figure 2). DBs of *fhod-1( ); cyk-1(ts)* mutants consistently appeared partially dispersed, as in *fhod-1( )* mutants, again with no deficient areas (Figure 2). Our data suggest that constitutive absence of either FHOD-1 or CYK-1, but not post-embryonic loss of CYK-1, results in abnormal DB morphology.

Absence of FHOD-1 but not acute loss of CYK-1 partially disrupts sarcomere structure in embryonic BWM.

Lack of major BWM effects after post-embryonic loss of CYK-1 led us to hypothesize that the more severe defects in *cyk-1( )* mutants might be due to CYK-1 deficiency during embryogenesis. To test this, we used the *cyk-1(ts)* to induce acute CYK-1 loss during embryonic myogenesis. To allow identification of BWM in embryos, we crossed into the formin mutants GFP-tagged muscle myosin II heavy chain A (GFP::MYO-3) (Campagnola et al., 2002), which is expressed in BWM.

Development of embryonic BWMs is reflected in characteristic changes in appearance of muscle components (Figure 3) (Hresko, Williams, & Waterson, 1994). After gastrulation, *C. elegans* embryos develop through stages called pre-bean, bean, comma, 1.5-fold, 2-fold, and 3-fold, named after the changing shape of the embryo. At 290 min after first cell division, equivalent to a pre-bean stage, myoblasts appear at lateral positions and accumulate diffuse myosin. By 350 min, the comma stage, myoblasts complete migration to dorsal and ventral quadrants, and muscle components start to polarize at the cell edges towards the hypodermis (Figure 3, Figure 4 A). At 420 min, the 1.5-fold stage, muscle cells flatten and F-actin and myosin assemble into the contractile lattice, with a polarized accumulation at cell-cell junctions between myoblasts (Figure 3). At 450 min, the 2-fold stage, functional sarcomeres have formed (Figure 3), and muscle-muscle and muscle-hypodermis junctions assemble. In stages older than 2-fold, sarcomeres become more neatly organized into striations (Figure 3, Figure 5 A).

To examine embryonic myoblasts, we obtained pools of mixed-stage embryos by bleaching adult worms grown at permissive temperature, liberating embryos from the adult bodies. We allowed this asynchronous population to continue developing at permissive temperature until the percentage of embryos at the two-fold stage peaked in each individual pool. Embryos were maintained a further 30 min either at permissive or restrictive temperature before staining with fluorescent phalloidin.

We assigned embryos to two broad age categories: early embryonic stages encompassing comma to 1.5-fold, and late embryonic stages including 2-fold and older. Based on the timing of muscle development, we expect younger embryos would normally have undergone

initial polarization of F-actin and myosin during the temperature shift. Consistent with this, a majority (~ 80%) of wild-type, *fhod-1( )*, and *cyk-1(ts)* early embryos had polarized BWMs. However, only 35% of *fhod-1( ); cyk-1(ts)* early embryos did so, with the remainder being nonpolarized (Figure 4 A, B), indicating *cyk-1* and *fhod-1* make a redundant contribution to early polarization of sarcomeric components. Surprisingly, *fhod-1( ); cyk-1(ts)* embryos maintained at permissive temperature had similar percentages of non-polarized BWM (Figure S3 A), suggesting this defect is not triggered by acute loss of CYK-1 function, but again consistent with *cyk-1(ts)* being partially non-functional at 16°C.

On reaching later stages (2-fold stage and older), embryos of all strains had striations of F-actin and myosin, whether or not they were shifted to restrictive temperature, suggesting absence of polarization in early embryos was temporary. However, these F-actin-rich striations appeared frayed in some late embryos (Figure 5 A). Again, the proportion varied by genotype, with roughly 75% of wild-type or *cyk-1(ts)* older embryos appearing normal, whereas only ~ 10–15% *fhod-1( )* or *fhod-1( ); cyk-1(ts)* embryos did so, the remaining 85–90% having frayed F-actin (Figure 5 B, Figure S3 B). Thus, absence of FHOD-1 but not acute loss of CYK-1 perturbs sarcomere organization in late embryogenesis.

In order to verify *cyk-1(ts)* was behaving as a loss of function allele under these test conditions, we also maintained populations of embryos at restrictive temperature overnight before fixation and staining with fluorescent phalloidin. We observed in some *fhod-1( ); cyk-1(ts)* L1 larvae a temperature-sensitive detachment of the pharynx from the mouth (38% of animals at 26°C, versus 13% at 16°C, n = 100 animals per condition) (Figure S4 A), a phenotype we have previously noted with *fhod-1( ); cyk-1( )* mutants or after RNAi against *cyk-1* on *fhod-1( )* mutants (Mi-Mi et al., 2012). In contrast, we never observed this in wild-type or *cyk-1(ts)* animals (n = 100 animals per strain per condition), and very rarely in *fhod-1( )* animals (3% of animals at 16°C, 4% at 26°C, n = 100 animals per condition). Thus, *cyk-1(ts)* replicated *cyk-1* loss-of-function phenotypes previously observed. Unexpectedly, we also observed accumulation of F-actin in many nuclei of *cyk-1(ts)* and *fhod-1( ); cyk-1(ts)* embryos at permissive and restrictive conditions (Figure 4 A, arrowheads, Figure S4 B, C), but the significance of this is not clear. Overall, our data suggest FHOD-1 promotes proper F-actin organization in late embryonic BWM sarcomeres, while CYK-1 is redundant with FHOD-1 in a non-essential role only during initial stages of sarcomerogenesis.

FHOD-1 promotes BWM cell growth and proper DB organization in a cell-autonomous manner, whereas CYK-1 does not.

Despite the fact *cyk-1( )* mutants exhibit significant BWM cell size and DB defects, our results here suggested CYK-1 makes minimal contributions to embryonic or post-embryonic BWM sarcomere assembly. One potential explanation for this discrepancy is that CYK-1 might promote BWM development indirectly by playing a role in some other tissue that affects BWM. Further, it remained formally possible FHOD-1 also works in a similar indirect manner. Thus, we tested whether re-expression of FHOD-1 or CYK-1 could support BWM development in a muscle cell autonomous manner in *fhod-1( )* and *cyk-1( )* mutants, as would be expected if either directly contributes to sarcomere assembly.

We had previously demonstrated *fhod-1(+)* genomic sequence with an encoded C-terminal GFP tag (denoted *fhod-1::gfp*) partially restores BWM growth in *fhod-1( )* animals when integrated at an exogenous genomic site (Mi-Mi et al., 2012). We had also observed genomic integration of *cyk-1::gfp* derived from genomic *cyk-1(+)* sequence rescues normal body size and partially rescues fertility of homozygous *cyk-1( )* animals (Mi-Mi et al., 2012). We phalloidin stained age-matched wild-type, *cyk-1( )*, and transgene-rescued *cyk-1( )*; *cyk-1::gfp* adult animals, and confirmed this exogenous *cyk-1* also restores normal BWM growth to *cyk-1( )* mutants (Figure S5).

To test for whether BWM rescue occurs in a cell autonomous manner, we took advantage of the ability of *C. elegans* to host extrachromosomal arrays (ECAs) that tend to be inherited in a mosaic manner (Mello, Kramer, Stinchcomb, & Ambros, 1991). When plasmids are microinjected into the worm gonad, they are linearized and concatenated into ECAs. ECAs can be inherited through multiple generations of progeny, but often variably among cells within an embryo to produce mosaic animals.

To induce mosaic *fhod-1* expression, we microinjected homozygous *fhod-1( )* worms with plasmid bearing *fhod-1(+)* genomic sequence. To avoid potential interference from tags, we utilized the original untagged gene from which the GFP-tagged version had been created (Mi-Mi et al., 2012). To facilitate identifying transgenic BWM cells in transformed animals, we co-injected a plasmid encoding free GFP expressed from the muscle-specific *myo-3* promoter. Concatenation of these plasmids into a single ECA ensured BWM cells expressing free GFP had also inherited *fhod-1(+)* (Figure 6 A). For analysis, we selected two independent transformant lines. To generate controls for the effects of harboring an ECA, we also injected *fhod-1( )* animals with a mixture of non-formin DNA and the GFP-encoding plasmid, and isolated two transformant lines. Similarly, to induce mosaic *cyk-1* expression, we injected untagged genomic *cyk-1(+)* or non-formin DNA, together with *gfp*-coding plasmid. However, as *cyk-1( )* homozygotes are sterile, this was done into heterozygous *cyk-1( )/+* worms.

Synchronized adult mosaic worms were stained with phalloidin, and widths of individual adjacent GFP-positive (transgenic) muscle cells and GFP-negative (non-transgenic) muscle cells were measured (Figure 6 A). As expected, there were no significant differences between GFP-positive and GFP-negative cells of control strains in either background (Figure 6 B, C). However, in *fhod-1( )* mutants with mosaic *fhod-1* expression, *fhod-1(+)*-bearing GFP-positive muscle cells were significantly wider than non-GFP neighbors (Figure 6 B), demonstrating FHOD-1 can promote muscle cell growth in a cell autonomous manner.

To test whether *cyk-1* similarly promotes muscle cell growth, we identified homozygous *cyk-1( )* progeny of heterozygous *cyk-1( )/+* parents by the presence of protruding vulva and/or absence of embryos from the gonad, and examined BWM cells in these animals after phalloidin stain. In contrast to *fhod-1*, widths of GFP-positive muscle cells expressing *cyk-1(+)* and GFP-negative cells not expressing *cyk-1(+)* were the same as each other, and as in non-transformed *cyk-1( )* worms (Figure 6 C), suggesting CYK-1 cannot promote BWM growth in a muscle cell autonomous manner.

Considering these results, we wanted to determine if FHOD-1 could also rescue DB organization in a cell autonomous manner. To test this, we immunostained the same mosaic *fhod-1( )* strains with anti-GFP and anti-ATN-1, and quantitatively analyzed the regularity of DB spacing along striations by performing fast Fourier transform (FFT) on anti-ATN-1 intensity profiles. Consistent with a fairly regular DB spacing in wild-type animals, amplitude spectra for their DBs showed a clustering of peaks near frequencies 0.8–1.0 μm^{-1}, whereas irregularly spaced ATN-1 in *fhod-1( )* mutants correlated with spectra with no particular favored frequency (Figure 7, Figure S6). As expected, in *fhod-1( )* strains transformed with non-formin DNA, DBs of GFP-positive (transgenic) and GFP-negative (non-transgenic) BWM cells were irregular in shape and spacing, identical to non-transgenic *fhod-1( )* mutants, and their amplitude spectra showed no favored frequency (Figure 7, Figure S6). In contrast, DBs in GFP-positive *fhod-1(+)*-expressing cells in the two *fhod-1* mosaic strains were regularly spaced, similar to wild type, and their spectra peaks clustered near 0.8–1.0 μm^{-1} (Figure 7, Figure S6). Notably, neighboring GFP-negative (non-transgenic) cells in these same animals resembled those of non-transformed *fhod-1( )* mutants, confirming FHOD-1 promotes proper DB organization in a muscle cell autonomous manner.

FHOD-1 is enriched near sarcomeres in growing BWM cells throughout development, whereas CYK-1 does not localize to the BWM contractile lattice.

Our results so far indicated FHOD-1 contributes to BWM sarcomere organization throughout embryonic and postembryonic development. Previously, we had observed FHOD-1 localizes in a diffuse pattern in BWM during late embryogenesis after F-actin rich sarcomeres had assembled (older than 2-fold stage), and becomes enriched at BWM cell edges from mid larval development until early adulthood (Mi-Mi et al., 2012). Considering evidence here for FHOD-1 function during earlier embryonic muscle development, we re-examined its distribution in embryos and young larvae expressing a rescuing FHOD-1::GFP, after staining with fluorescently-labeled phalloidin to identify BWMs. Expanding on our previous results, we observed FHOD-1::GFP in BWMs of animals from embryonic 1.75 fold stage through L1 (Figure 8). FHOD-1 localized diffusely in younger stage embryonic BWM when sarcomeric components start to polarize and assemble into sarcomeres, and gradually appeared more punctuate at the edges of the F-actin-rich contractile lattices from later embryogenesis through early larval development, when sarcomeres mature. Similar patterns of fluorescence were visible in live embryos and larvae expressing FHOD-1::GFP (Figure S7). Thus, FHOD-1 is present through all stages of BWM development when sarcomere assembly is occurring.

Our results here also suggest CYK-1 plays no direct role in sarcomere formation, and that strong BWM defects in *cyk-1( )* mutants reflect indirect contributions. This was surprising in light of previous evidence CYK-1 localizes to DBs, and thus we also re-examined CYK-1 localization. We had previously observed that when expressed from multiple copies of a transgene on an ECA, CYK-1::GFP appears along striations as puncta that resembled DBs (Mi-Mi et al., 2012). However, that transgenic line lost the unstable ECA before we were able to compare the CYK-1::GFP puncta to a bona fide DB marker. We had also previously examined the homozygous *cyk-1( )* worms bearing *cyk-1::gfp* integrated in the genome that

partially rescued fertility and fully rescued body morphology and BWM growth (Mi-Mi et al., 2012; Figure S5). In that case, we had not observed any BWM-associated GFP fluorescence (Mi-Mi et al., 2012), but had speculated the transgene might only be partially functional based on its limited ability to rescue fertility.

To avoid these issues, we examined here GFP fluorescence in a strain in which the endogenous *cyk-1* locus had been tagged with *gfp* using CRISPR-Cas9, resulting in a *cyk-1::gfp* that is functional for its essential role during embryogenesis (Davies et al., 2018). As expected, we observed CYK-1:: GFP localized in the germline similar to endogenous CYK-1 (Severson, Baillie, & Bowerman, 2002; Figure S8 A). BWM appeared grossly normal in these animals, and we did not observe CYK-1::GFP at any structure in BWM, including DBs (Figure S8 B). We also examined a strain expressing CYK-1::GFP from an independently isolated ECA (Shaye & Greenwald, 2016), and observed punctate GFP-positive structures in BWM, but these were not positioned along the muscle I-bands or with any regularity, indicating these were not DBs (Figure S8 C). Rather, these might represent aggregates that arose due to CYK-1::GFP over-expression from the ECA.

We had also previously observed anti-CYK-1 stains DBs in BWM (Mi-Mi et al., 20120). Considering our negative results here, we tested the specificity of our previous CYK-1 immunostain. To eliminate CYK-1, we performed *cyk-1(RNAi)* for 5 days on a strain with enhanced sensitivity to RNAi due to a mutation in the exoribonuclease gene *eri-1* (Pavelec et al., 2009). As a control to verify the efficacy of *cyk-1(RNAi)*, we also treated the strain in which endogenous *cyk-1* had been tagged with *gfp* (Davies et al., 2018). Consistent with efficient knockdown, *cyk-1(RNAi)*-treated worms were sterile. Western blot analysis using the same anti-CYK-1 from our previous study showed reactive bands close to predicted molecular weights for CYK-1 (arrows) and for CYK-1::GFP (arrowheads) were eliminated from *cyk-1(RNAi)*-treated animals (Figure 9 A). Immunostain of adults with that same antibody decorated the germline in controls (arrowheads) but not *cyk-1(RNAi)* animals (Figure 9 B). In contrast, strong immunostain of DBs in adult BWM using with this anti-CYK-1 (counter-stained for MYO-3 to identify BWM, not shown) was not lost in *cyk-1(RNAi)*-treated animals (Figure 9 C). Thus, DB stain in BWM from anti-CYK-1 is likely non-specific. The nature of this DB-associated antigen is unclear, but we think it is unlikely to be another formin based on our previous inability to detect cross-reactivity of this antibody to other worm formins (Mi-Mi et al., 2012). These results suggest CYK-1 does not localize to DBs or any other sarcomeric structure in BWM, consistent with this formin playing no direct role in promoting sarcomere formation.

Discussion

Formin contributions to sarcomere organization during striated muscle development have been documented across various model systems, but their precise roles in this are unclear (Sanger et al., 2017). The striated body wall muscle (BWM) of *C. elegans* is a powerful system to explore this due to the worm's smaller formin complement, which avoids potential redundancy due to multiple isoforms of each formin family in vertebrates. Despite this simplicity, there is remarkable similarity between sarcomeres of BWM and vertebrate cardiac muscle (Benian & Epstein, 2011).

A compelling hypothesis has been that formins initiate thin filament assembly owing to the tendency of many formins to assemble long, unbranched actin filaments associated with tropomyosin. We aimed to test that hypothesis using *C. elegans*, starting from our initial observations that simultaneous reduction of activity of two worm formins, FHOD-1 and CYK-1, profoundly stunts BWM development (Mi-Mi et al., 2012). Worms simultaneously bearing deletion alleles *fhod-1( ); cyk-1( )* produce small BWM cells with a highly reduced number of sarcomeres, a phenotype that might be considered consistent with formins initiating thin filament assembly. However, the requirement of CYK-1 for embryonic cell divisions made necessary the maternal rescue of *cyk-1( )* (i.e. inheritance of CYK-1 protein/mRNA from a parent), complicating this earlier analysis. Recent isolation of a conditional *cyk-1(ts)* (Davies et al., 2014) provided means to more fully eliminate CYK-1 activity after the critical window during embryogenesis had passed, without the complication of maternal inheritance.

Contrary to our expectations, analysis of *cyk-1(ts)* mutants suggested CYK-1 plays, at best, a very minor role in BWM growth during larval development. Muscle cell growth is driven by the assembly of additional sarcomeres, the majority of which occurs during larval development. Despite this, maintenance of developing *cyk-1(ts)* mutant larvae at a temperature where CYK-1 is non-functional caused almost no change in muscle cell growth, particularly when controlled for effects on overall body growth (Figure 1). Even when *cyk-1(ts)* was paired with *fhod-1( )*, rates of muscle cell growth were essentially identical to larvae bearing just *fhod-1( )*.

Similarly, BWM Z-line defects of *cyk-1( )* mutants were not recapitulated in *cyk-1(ts)* animals. In electron micrographs, wild-type dense bodies (DBs, the BWM Z-line analogs) appear as electron-dense finger-like projections, but many DBs in *cyk-1( )* mutants appear deficient in electron-dense material (Mi-Mi & Pruyne, 2015). Correspondingly, DBs of wild-type animals appear as ATN-1 (α-actinin)-rich puncta by immunostain, but many regions of *cyk-1( )* BWM lack apparent ATN-1-stained DBs (Figure 2). Conversely, DBs of *cyk-1(ts)* mutants grown at a restrictive temperature throughout larval development appear normal (Figure 2), again despite most DBs having assembled during the restrictive period. FHOD-1 absence also affects DB morphology (discussed below), but pairing of *cyk-1(ts)* with *fhod-1( )* did not produce a more severe phenotype than *fhod-1( )*, alone (Figure 2).

We suspected these differences in phenotypes between *cyk-1( )* and *cyk-1(ts)* mutants might be due to differences in the timing of CYK-1 loss. That is, through temperature control we restricted loss in *cyk-1(ts)* mutants to post-embryonic development, whereas CYK-1 loss presumably begins earlier in *cyk-1( )* mutants with depletion of maternal product. The more severe *cyk-1( )* effects might therefore imply that CYK-1 contributes to BWM formation earlier in development. However, using the *cyk-1(ts)* we were unable to find evidence for a significant CYK-1 role in embryonic BWM sarcomere formation. We did observe that compared to wild-type or single mutant strains, a larger percentage of *fhod-1( ); cyk-1(ts)* double mutant embryos were delayed in the initial accumulation of F-actin and myosin at the start of sarcomere formation (Figure 4). However, as sarcomeres are present in two-fold stage *fhod-1( ); cyk-1(ts)* embryos, we reasoned this early polarization defect is probably

temporary, and *cyk-1(ts)* had no effect on the appearance of sarcomeres in older embryos (Figure 4).

One caveat to interpreting results using the *cyk-1(ts)* is that it is possible the temperature-sensitive CYK-1 protein does not actually lose function in BWM. For example, the mutant protein might somehow be stabilized in BWM cytoplasm, or its role in BWM may rely on a biochemical activity or protein-protein interaction distinct from those required for cytokinesis. Thus, we used the alternative approach of examining *cyk-1( )* mutants, which should lack all FH2-dependent functions of CYK-1, and which do exhibit strong BWM defects. We confirmed genomic integration of a *cyk-1* transgene fully rescues BWM defects of *cyk-1( )* animals (Figure S5), demonstrating those defects are specific to loss of CYK-1. However, when a similar *cyk-1* transgene was inherited in a mosaic pattern in *cyk-1( )* animals, we failed to observe cell autonomous rescue of BWM growth (Figure 6 C). Even more surprising, we also saw no evidence of non-cell autonomous rescue of BWM cell growth in these mosaic *cyk-1*-expressing animals. That is, we might have expected all BWM cells of mosaic *cyk-1* animals would be larger than in *cyk-1( )* controls lacking the transgene. However, we observed no difference in BWM cell size between those strains (Figure 6 C). We therefore suggest that *cyk-1* function may be required simultaneously in many cells, which would occur only rarely in a mosaic strain, or that it may be required in a tissue where expression of non-integrated transgenes is weak, such as the germline (Mello et al., 1991).

Our overall results, together with inability to detect CYK-1 in BWM sarcomeres (Figure 9, Figure S8), suggest CYK-1 plays an indirect role in BWM development. That is, CYK-1 in some other tissue(s) indirectly promotes muscle development. Based on our *cyk-1(ts)* observations, we suggest this function likely occurs during early embryogenesis, possibly before myoblasts begin sarcomere formation. Consistent with this possibility, CYK-1 functions in a variety of tissues other than BWM, and *cyk-1( )* or *cyk-1(RNAi)*-treated animals also exhibit defects in germline, epidermis, intestine, and excretory canal (Swan et al., 1998; Mi-Mi et al., 2012; Shaye & Greenwald, 2016; Gong et al., 2018). We also observed that embryos bearing *cyk-1(ts)* accumulate F-actin in many nuclei (Figure 4 A, Figure S4 B, C), indicating loss of CYK-1 has effects throughout the body during early embryogenesis. Thus, we suggest BWM phenotypes of *cyk-1( )* and *cyk-1(RNAi)*-treated animals are a secondary consequence of some function not directly related to sarcomere formation in BWM.

In contrast, FHOD-1 seems to promote BWM development and Z-line organization directly. FHOD-1 is initially diffuse in embryonic BWM cells, when sarcomeric components begin to accumulate at the cell membrane. Once the initial sarcomeres have formed, the formin appears as puncta at BWM cell edges, and more diffusely along sarcomere I bands (Figure 7), remaining so until the end of BWM growth in adulthood, when localized formin is no longer detected (Mi-Mi et al., 2012). In embryos, lack of FHOD-1 results frayed-appearing F-actin in the newly formed sarcomeres (Figure 5, Figure S4), suggesting a partial defect in thin filament anchorage and organization. In larvae lacking FHOD-1, additional sarcomere assembly in BWM cells is slow, resulting in smaller BWM cells (Figure 1, Figure S1) (Mi-Mi et al., 2012). In contrast to CYK-1, mosaic expression of FHOD-1 in *fhod-1( )* mutants

promotes BWM growth in a cell autonomous manner (Figure 6 B). We note rescue is not complete (Figure 6 B, compare wild-type to GFP-positive *fhod-1*), but it is unclear whether this reflects an additional non-cell autonomous effect or just an artifact of gene expression from an ECA. FHOD-1 also promotes proper DB organization in a cell autonomous manner. That is, where DBs are of irregular size and spacing in *fhod-1( )* adults (Mi-Mi et al., 2012), mosaic FHOD-1 expression restores regular, punctate DB organization in transgenic cells (Figure 7, Figure S6). These results suggest the ability of FHOD-1 to promote BWM cell growth and proper DB organization are direct effects that may be functionally linked.

We have found no evidence any other formin contributes to BWM development in worms, either from individual formin gene mutations, or from pairing of *fhod-1( )* with mutations in each of the remaining non-*cyk-1* formins (Figure S2) (Mi-Mi et al., 2012). One caveat to this is possibility of a higher degree of redundancy among formins, with simultaneous elimination of more (or all) worm formins resulting in a stronger BWM phenotype. However, absence of even hints of synthetic defects in BWM development between *fhod-1( )* and other non-*cyk-1* formin mutations makes this unlikely. Thus, we suggest *fhod-1( )* BWM cells lack any formin activity that contributes directly to sarcomere formation. And as *fhod-1( )* BWM cells contain abundant thin filaments, we think it unlikely that thin filament assembly in *C. elegans* BWM requires formins. It is possible this differs in vertebrate or fly muscle, and that formins assemble their thin filaments. However, vertebrate muscle contains non-formin actin nucleating factors that might initiate thin filament assembly, including leiomodins (Chereau et al., 2008; Yuen et al., 2014; Boczkowska, Rebowski, Kremneva, Lappalainen, & Dominguez, 2015) and a complex of N-WASP with nebulin (Takano et al., 2010). Worms lack unambiguous leiomodin and nebulin homologs, but they host related proteins, and other unknown actin nucleation factors could initiate their thin filament assembly.

A novel result from our study is that formins have only a modest effect on muscle development in the worm. Loss of DAAM-family formins significantly perturbs sarcomere organization in mammalian and insect muscle (Molnár et al., 2014; Ajima et al., 2015), but worm DAAM-1 appears dispensable (Figure S2). Absence of FHOD-1, the only *C. elegans* representative of FHOD-family, results in muscle defects much milder than the well-studied impacts of FHOD-family members in other systems (Taniguchi et al., 2009; Iskratsch et al., 2010; Kan-O et al., 2012; Shwartz et al., 2016; Ushijima et al., 2018; Fenix et al., 2018). For example, where *fhod-1( )* worms exhibit reduced sarcomere assembly and partially defective Z-lines/DBs, knockdown of FHOD3 in human induced pluripotent stem cell-derived cardiomyocytes blocks the maturation of stress fiber-like structures into sarcomere-containing myofibrils (Fenix et al., 2018), phenotypes that appear to recapitulate those of the *fhod3*$^{-/-}$ mouse heart (Kan-O et al., 2012). Moreover, where *fhod-1( )* BWM is largely functional and mutant worms are fully viable, mice lacking FHOD3 die during embryonic development due to heart failure (Kan-O et al., 2012).

It is not immediately clear why worm muscle should be so resilient to formin loss as compared to other organisms. One possible explanation is the unique architecture of its contractile machinery. Sarcomeres in mammalian and *Drosophila* striated muscles organize into myofibrils, most of which are suspended in the cytoplasm away from the plasma

membrane. Conversely, all *C. elegans* BWM sarcomeres are directly anchored to the plasma membrane and the underlying extracellular matrix through integrin-based adhesions. This likely provides significant mechanical reinforcement. This might, for example, permit DBs in worm muscle to tolerate structural defects that would be catastrophic for Z-lines in myofibrils. The mechanisms for precisely how mammalian FHOD3 or worm FHOD-1 promotes sarcomere formation are not understood, but the relative resilience of worm muscle to loss of its FHOD-family formin may prove to be an advantage in dissecting details of this process.

Materials and Methods

Worm strains and growth conditions

Worms were grown using standard protocols (Brenner, 1974) at 20°C, except for experiments involving temperature-sensitive worms, for which growth was at 16°C prior to temperature shifts. Age-synchronized populations were obtained in one of two ways. By one method, adult worms were treated with 1:2 ratio 5 M NaOH to reagent grade bleach to liberate embryos, which were then washed with M9 medium (Ausubel et al., 2002), and allowed to develop until the proportion at two-fold stage had peaked (Figures 3, 4, 5, S3, S4), or until hatching into starvation-arrested L1 stage larvae (Figures 1, 2, 8, 9, S1, S4). Alternatively, adults were allowed to lay eggs on plates for ~ 4–8 hrs and then removed, resulting in semi-synchronized progeny (Figures 6, 7, S2, S5, S6, S8).

For long temperature shift experiments (Figures 1, 2, S1), starvation-arrested L1s were introduced to food (*Escherichia coli* OP50) at permissive (16°C) or restrictive (26°C) temperature for 0–72 hrs before being prepared for fluorescence microscopy. For short temperature shift experiments (Figures 4, S3, S4), embryos in M9 were transferred to 16°C or 26°C water baths for 30 min before preparation for fluorescence microscopy.

For complete genotypes of strains used in this study, see Table 1. N2 (wild-type Bristol worms) and RW1596 [*myo-3(–); gfp::myo-3*] were supplied by the *Caenorhabditis* Genetics Center (University of Minnesota, Minneapolis, MN). JCC389 [*cyk-1(ts)*] and JCC955 [*cyk-1::gfp*] were gifts from Julie Canman (Columbia University, New York, NY; Davis et al., 2014; Davies et al., 2018). GS7933 [*Ex[cyk-1::gfp]*] was a gift from Daniel Shaye (University of Illinois at Chicago, Chicago, IL; Shaye & Greenwald, 2016). XA8001 [*fhod-1( )*], DWP8 [*cyk-1( )/+*], DWP9 [*fhod-1( ); cyk-1( )/+*], DWP10 [*fhod-1( ); fhod-1::gfp*], DWP22 [*cyk-1( ); cyk-1::gfp*], and DWP28 [*eri-1(–)*] were obtained previously (Mi-Mi et al., 2012). Parentage of strains produced for this study are in Table 1.

Novel loss-of-function allele *daam-1(ups39)* was generated using CRISPR/Cas9-mediated gene editing to target TAATTGACCCGAGACGCTAT near the start of an FH2-coding exon of *daam-1*. Homologous recombination-guided repair was directed using a template constructed as follows. Nucleotides 22,974 – 24,147 of *daam-1* was amplified by PCR with appended upstream *KpnI* cloning site, and downstream *EcoRI* site, in-frame stop codon, *LoxP*, and *SalI* cloning site (primers GGTACCGAGCGGATTGCAAAAGAGCTGGA and GTCGACATAACTTCGTATAATGTATGCTATACGAAGTTATTCAGAATTCGGTGATCT GGAAATGAAAGTTGTATAC), and nucleotides 24,198 – 25,339 of *daam-1* were amplified

and appended with upstream *BamHI* cloning site and *LoxP*, and downstream *NotI* cloning site (primers GGATCCATAACTTCGTATAGCATACATTATACGAAGTTATAACTGCACAATAATGCT CTCCAAGC and GCGGCCGCTCTACCCACCTCATACCTACACGC). These were sequentially cloned into pJKL702 (a gift from Jun Kelly Liu, Cornell University, Ithaca, NY) to flank its *unc-119* mini-gene to create the homologous recombination-guided repair template. We generated and isolated transgenic lines from HT1593 [*unc-119(−)*] animals, and subsequently excised the integrated *unc-119(+)* from the *daam-1* locus by expression of Cre recombinase, all as described by others (Dickinson & Goldstein, 2016). The resultant post-excision *daam-1(ups39)* encodes an in-frame stop codon near the start of its FH2-coding sequence, and a 1-nt frame shift due to the *LoxP* site, and is thus predicted encode a non-functional formin. DWP219 [*daam-1(−)*] was generated by crossing *daam-1(ups39)* into an *unc-119(+)* background, using EcoRI-mediated cleavage as a diagnostic for *ups39*.

To generate worms with mosaic expression of *fhod-1*, young adult XA8001 hermaphrodites were microinjected with a mixture of 50 ng/μL pRS315-*fhod-1(+)* (Mi-Mi et al., 2012), 100 ng/μL *rab-3p::gfp* plasmid, 50 ng/μL *myo-3p::gfp* plasmid, and 25 ng/μL *myo-2p::gfp* plasmid. Two independent strains (DWP199, DWP202) were isolated from progeny of different injected parents based on mosaic expression of GFP in BWM. Two control strains (DWP204, DWP206) with mosaic transgene inheritance but lacking *fhod-1(+)*, were produced similarly, but replacing pRS315-*fhod-1(+)* with pRS315 (Sikorski & Hieter, 1989). To isolate animals with mosaic expression of *cyk-1*, DWP153 [*cyk-1( )/+*] worms were microinjected with 50 ng/μL pRS315-*cyk-1(+)* or pRS315, and 100 ng/μL *rab-3p::gfp* plasmid, 50 ng/μL *myo-3p::gfp* plasmid, and 25 ng/μL *myo-2p::gfp* plasmid, to generate test strains (DWP208, DWP209) and control strains (DWP211, DWP213) as above.

RNAi

RNAi-mediated knockdowns were performed by the standard feeding technique (Wang and Barr, 2005). Briefly, *E. coli* HT115 was transformed with control knockdown vector L4440 (Timmons & Fire, 1998) or *cyk-1* knockdown vector L4440-*cyk-1* (Mi-Mi et al., 2012), and grown overnight at 37°C in 2xYT (Ausubel et al., 2002) with 12.5 μg/ml tetracycline, 100 μg/ml ampicillin. Cultures were diluted 1:100 in 2xYT, grown 3 hrs 37°C, and induced 3–4 hrs with 0.4 mM IPTG at 37°C before concentrating five-fold and seeding onto agar. Age-synchronized L1 worms were introduced and grown 3–4 days at 25°C, then washed as adults using M9 to remove progeny, and introduced to freshly induced bacteria to continue RNAi knockdown for 5 days total.

Staining for fluorescence microscopy

F-actin stain was as previously described (Mi-Mi et al., 2012), as was immunostain (Finney & Ruvkun, 1990), except for omission of spermidine-HCl from the initial buffer for both protocols, and threefold higher initial methanol concentration (75%) for immunostain. For the specific case of *cyk-1* mosaic worms (Figures 6 C), poor transmittance of *cyk-1* ECAs prevented harvesting large batches of transgenic animals. Instead, individual animals were picked and stained directly on glass slides, as previously (Hegsted, Wright, Votra, & Pruyne, 2016), with staining performed overnight. Monoclonal primary antibody MH35 (anti-

ATN-1) generated by R.H. Waterston (Francis & Waterston, 1985) was a gift from Pamela Hoppe (Western Michigan University, Kalamazoo, MI), polyclonal rabbit anti-GFP was a gift from Anthony Bretscher (Cornell University, Ithaca, NY), polyclonal affinity-purified anti-CYK-1 (DPMSP1) was generated previously (Mi-Mi et al., 2012), mouse anti-GFP and secondary antibodies (Texas red-conjugated goat anti-rabbit and FITC-conjugated goat anti-mouse, or reverse fluorophore/species) were purchased (Rockland Immunochemicals, Pottstown, PA). Antibody dilutions were 1:200 DPMSP1, $1:10^4$ MH35, $1:10^3$ mouse anti-GFP, 1:200 rabbit anti-GFP, and 1:500 for secondary antibodies.

Microscopy and image analysis

Wide field fluorescence images (Figures 1, 4, 5, 6, 9 B, C, S2, S4 A, B, S5, S7 A) were acquired using an Eclipse 90i Upright Research Microscope (Nikon, Tokyo, Japan) at room temperature (~25°C) with a CFI Plan Apochromat 40x/NA 1.0 oil immersion objective, or a CFI Plan Apochromat violet-corrected 60x/NA 1.4 oil immersion objective, with a Cool-SNAP HA2 digital monochrome charge-coupled device camera (Photometrics, Tucson, AZ) driven by NIS-Elements AR acquisition and analysis software (version 3.1; Nikon, Tokyo, Japan). Confocal images (Figures 2, 3, 7, 8, S4 C, S7, S8 B, C) were obtained on an SP8 Laser Scanning Confocal Microscope (Leica, Wetzlar, Germany) driven by LAS X Software (version 2.2.0, build 4758; Leica, Wetzlar, Germany), and using an HCX Plan Apochromat 63x/NA 1.4 oil lambda objective. Maximum intensity projections and XZ cross-sections were generated from confocal stacks using LAS X Software or ImageJ (version 2.0.0-rc-65/1.51g) (Schneider, Rasband, & Eliceiri, 2012). Images were linearly processed to enhance contrast and false-colored in Photoshop CS4 or CC 2018 (Adobe, San Jose, CA).

BWM and muscle cell widths were measured based on phalloidin stain, and total body width was measured based on body autofluorescence in the FITC channel using NIS-Elements AR, as previously (Mi-Mi et al., 2012). Embryonic developmental stages were visually identified based on embryo shape, and BWMs were identified by GFP::MYO-3 (see results, Figures 3, 4, 5). In animals with mosaic expression of soluble GFP in muscle cells, the FITC-channel was used to identify adjacent green and non-green muscle cells, followed by measurement of cell width based on phalloidin stain or analysis of DB organization based on ATN-1 immunostain (Figures 6, 7, S6). To examine BWM cells in homozygous *cyk-1( )* progeny of heterozygous *cyk-1( )/+* parents (Figure 6), such progeny were identified by presence of protruding vulva and/or absence of embryos from the gonad (Mi-Mi et al., 2012). For examination of CYK-1 immunostain after *cyk-1(RNAi)* (Figure 9), animals negative for anti-CYK-1 germline stain were selected as verification of efficient knockdown of CYK-1. Fluorescence images for comparison between *cyk-1(RNAi)* and control (Figure 9) were consistently acquired at 500 ms exposures. All quantitative analyses were performed while blinded to the strain genotype, except for analysis of strains examined for Figure 6 C (*cyk-1* mosaic analysis), which due to poor propagation of *cyk-1*-containing ECAs across generations, were collected, stained, and analyzed as transgenic individuals became available over several weeks.

Fast Fourier transform (FFT)

Anti-ATN-1 stain intensity profiles were obtained for approximately eight DB-containing striations in one GFP-positive (ECA-containing) muscle cell and one adjacent GFP-negative (ECA-lacking) muscle cell each in ten mosaic animals of each strain (as seen in Figure 7), using Freehand Line tool in ImageJ. There are relatively few DBs per striation, and their spacing is somewhat variable, producing a weak signal after FFT. To amplify this, intensity profiles were concatenated at peak maxima for ATN-1 (i.e. the last peak maximum of one profile was joined to the first peak maximum of the next). FFT was performed and amplitude spectra obtained using MATLAB (R2019a Update 2). Analyses were performed while blinded to strain genotypes.

Western blots

Whole worm lysates were obtained from age-synchronized young adults by washing worms off agar and separating from *E. coli* before concentrating in 1.7 mL tubes to a 1:1 worm to M9 slurry. Reducing sample buffer (2X) was directly added to samples before boiling 3 min, disruption 30 sec with tissue homogenizer (VWR International, Radnor, PA), boiling 3 min, and pelleting 15 sec. To break up genomic DNA, samples were pulled through an insulin syringe eight times before loading for SDS-PAGE. For purposes of normalization, samples were subject to preliminary SDS-PAGE and Coomassie brilliant blue stain. Images were acquired using a Bio-Rad ChemiDoc MP imager (Bio-Rad, Hercules, CA), and intensities of stain for total lanes were compared using Image Lab software (Bio-Rad, Hercules, CA). For western blot analysis, proteins in normalized samples were resolved by SDS-PAGE and transferred to nitrocellulose (Bio-Rad, Hercules, CA). Blots were blocked in 10% milk/ TBST (50 mM Tris-HCl, pH 8.3, 150 mM NaCl, 0.3% Tween 20) and incubated 5 hrs with DPMSP1 diluted 1:200 in TBST/1% milk, 5 hrs. Blots were washed and incubated 1 hr in goat anti-rabbit horseradish peroxidase-conjugated secondary antibody (Rockland Immunochemicals, Gilbertsville, PA) diluted 1:3000 in TBST/1% milk, before washing and treating with enhanced chemiluminescence substrate (ThermoFisher Scientific, Waltham, MA). Images were acquired using a Bio-Rad ChemiDoc MP imager, and processed with Image Lab and Photoshop CS4.

Statistical analyses

Numerical data are expressed as mean ± standard error of the mean or one standard deviation, as defined in the text. Graphs were made in Excel:windows (version 14.7.2; Microsoft Corporation, Redmond, WA). For results where two groups are compared (Figure 6), data were analyzed using a student t-test. For results from three or more groups, data were analyzed using Analysis of Variance, followed by a Least Significant Difference *post hoc* test. *P value* < 0.05 was considered to be statistically significant.

Data availability statement

Data supporting the findings of this study are available from the corresponding author upon reasonable request.

Supplementary Material

Refer to Web version on PubMed Central for supplementary material.

Acknowledgements:

References

Ajima R, Bisson JA, Helt J-C, Nakaya M-A, Habas R, Tessarollo L, He X, Morrisey EE, Yamaguchi TP, & Cohen ED (2015). DAAM1 and DAAM2 are co-required for myocardial maturation and sarcomere assembly. Developmental Biology, 408, 126–39. 10.1016/j.ydbio.2015.10.003 [PubMed: 26526197]

Arimura T, Takeya R, Ishikawa T, Yamano T, Matsuo A, Tatsumi T, Nomura T, Sumimoto H, & Kimura A (2013). Dilated Cardiomyopathy-Associated FHOD3 Variant Impairs the Ability to Induce Activation of Transcription Factor Serum Response Factor. Circulation Journal, 77, 2990–2996. 10.1253/circj.CJ-13-0255 [PubMed: 24088304]

Ausubel FM, Brent R, Kingston RE, Moore DD, Seidman JG, Smith JA, & Struhl K (2002). Short Protocols in Molecular Biology (5th ed.). United States: John Wiley & Sons.

Benian GM, & Epstein HF (2011). Caenorhabditis elegans muscle: A genetic and molecular model for protein interactions in the heart. Circulation Research, 109, 1082–1095. 10.1161/CIRCRESAHA.110.237685 [PubMed: 21998299]

Boczkowska M, Rebowski G, Kremneva E, Lappalainen P, & Dominguez R (2015). How leiomodin and tropomodulin use a common fold for different actin assembly functions. Nature Communications, 6, 8314 10.1038/ncomms9314

Brenner S (1974). The genetics of Caenorhabditis elegans. Genetics, 77, 71–94. [PubMed: 4366476]

Campagnola PJ, Millard AC, Terasaki M, Hoppe PE, Malone CJ, & Mohler WA (2002). Three-dimensional high-resolution second-harmonic generation imaging of endogenous structural proteins in biological tissues. Biophysical Journal, 82, 493–508. 10.1016/S0006-3495(02)75414-3 [PubMed: 11751336]

Chang F, Drubin D, & Nurse P (1997). cdc12p, a protein required for cytokinesis in fission yeast, is a component of the cell division ring and interacts with profilin. Journal of Cell Biology, 137, 169–182. 10.1083/jcb.137.1.169

Chereau D, Boczkowska M, Skwarek-Maruszewska A, Fujiwara I, Hayes DB, Rebowski G, Lappalainen P, Pollard TD, & Dominguez R (2008). Leiomodin is an actin filament nucleator in muscle cells. Science, 320, 239–243. 10.1126/science.1155313 [PubMed: 18403713]

Clark KA, McElhinny AS, Beckerle MC, & Gregorio CC (2002). Striated muscle cytoarchitecture: An Intricate Web of Form and Function. Annual Review of Cell and Developmental Biology, 18, 637–706. 10.1146/annurev.cellbio.18.012502.105840

Davies T, Jordan SN, Chand V, Sees JA, Laband K, Carvalho AX, Shirasu-Hiza M, Kovar DR, Dumont J, & Canman JC (2014). High-resolution temporal analysis reveals a functional timeline for the molecular regulation of cytokinesis. Developmental Cell, 30, 209–223. 10.1016/j.devcel.2014.05.009 [PubMed: 25073157]

Davies T, Kim HX, Romano Spica N, Lesea-Pringle BJ, Dumont J, Shirasu-Hiza M, & Canman JC (2018). Cell-intrinsic and -extrinsic mechanisms promote cell-type-specific cytokinetic diversity. ELife, 7, e36204 10.7554/eLife.36204 [PubMed: 30028292]

Dickinson DJ, & Goldstein B (2016). CRISPR-based methods for Caenorhabditis elegans genome engineering. Genetics, 202, 885–901. 10.1534/genetics.115.182162 [PubMed: 26953268]

Evangelista M, Blundell K, Longtine MS, Chow CJ, Adames N, Pringle JR, Peter M, & Boone C (1997). Bni1p, a Yeast Formin Linking Cdc42p and the Actin Cytoskeleton During Polarized Morphogenesis. Science, 276, 118–122. 10.1126/science.276.5309.118 [PubMed: 9082982]

Fenix AM, Neininger AC, Taneja N, Hyde K, Visetsouk MR, Garde RJ, Liu B, Nixon BR, Manalo AE, Becker JR, Crawley SW, Bader DM, Tyska MJ, Liu Q, Gutzman JH, & Burnette DT (2018). Muscle-specific stress fibers give rise to sarcomeres in cardiomyocytes. ELife, 7, e42144 10.7554/eLife.42144 [PubMed: 30540249]

Finney M, & Ruvkun G (1990). The *unc-86* gene product couples cell lineage and cell identity in *C. elegans*. Cell, 63, 895–905. 10.1016/0092-8674(90)90493-x [PubMed: 2257628]

Francis GR, & Waterston RH (1985). Muscle organization in *Caenorhabditis elegans*: localization of proteins implicated in thin filament attachment and I-band organization. Journal of Cell Biology. 101, 1532–1549. 10.1083/jcb.101.4.1532

Fujimoto N, Kan-O M, Ushijima T, Kage Y, Tominaga R, Sumimoto H, & Takeya R (2016). Transgenic expression of the formin protein fhod3 selectively in the embryonic heart: Role of actin-binding activity of fhod3 and its sarcomeric localization during myofibrillogenesis. PLoS ONE, 11, e0148472 10.1371/journal.pone.0148472 [PubMed: 26848968]

Gieseler K, Qadota H, & Benian GM (2017). Development, structure, and maintenance of *C. elegans* body wall muscle WormBook, ed. The *C. elegans* Research Community, WormBook 10.1895/wormbook.1.81.2

Gong T, Yan Y, Zhang J, Liu S, Liu H, Gao J, Zhou X, Chen J, & Shi A (2018). PTRN-1/CAMSAP promotes CYK-1/formin-dependent actin polymerization during endocytic recycling. The EMBO Journal, 37, e98556 10.15252/embj.201798556 [PubMed: 29567645]

Hayashi T, Tanimoto K, Hirayama-Yamada K, Tsuda E, Ayusawa M, Nunoda S, Hosaki A, & Kimura A (2018). Genetic background of Japanese patients with pediatric hypertrophic and restrictive cardiomyopathy. Journal of Human Genetics, 63, 989–996. 10.1038/s10038-018-0479-y [PubMed: 29907873]

Hegsted A, Wright FA, Votra S, & Pruyne D (2016). INF2- and FHOD-related formins promote ovulation in the somatic gonad of *C. elegans*. Cytoskeleton, 73, 712–728. 10.1002/cm.21341 [PubMed: 27770600]

Henderson CA, Gomez CG, Novak SM, Mi-Mi L, & Gregorio CC (2017). Overview of the Muscle Cytoskeleton. Comprehensive Physiology, 7, 891–944. 10.1002/cphy.c160033 [PubMed: 28640448]

Higgs HN, & Peterson KJ (2005). Phylogenetic Analysis of the Formin Homology 2 Domain. Molecular Biology of the Cell, 16, 1–13. 10.1091/mbc.e04-07-0565 [PubMed: 15509653]

Hresko MC, Williams BD, & Waterson RH (1994). Assembly of Body Wall Muscle and Muscle Cell Attachment Structures in *Caenorhabditis elegans*. Journal of Cell Biology, 124, 491–506. 10.1083/jcb.124.4.491

Imamura H, Tanaka K, Hihara T, Umikawa M, Kamei T, Takahashi K, Sasaki T, & Takai Y (1997). Bni1p and Bnr1p: Downstream targets of the Rho family small G-proteins which interact with profilin and regulate actin cytoskeleton in *Saccharomyces cerevisiae*. The EMBO Journal, 16, 2745–2755. 10.1093/emboj/16.10.2745 [PubMed: 9184220]

Iskratsch T, Lange S, Dwyer J, Kho AL, dos Remedios C, & Ehler E (2010). Formin follows function: A muscle-specific isoform of FHOD3 is regulated by CK2 phosphorylation and promotes myofibril maintenance. Journal of Cell Biology, 191, 1159–1172. 10.1083/jcb.201005060

Kan-O M, Takeya R, Abe T, Kitajima N, Nishida M, Tominaga R, Kurose H, & Sumimoto H (2012). Mammalian formin Fhod3 plays an essential role in cardiogenesis by organizing myofibrillogenesis. Biology Open, 1, 889–896. 10.1242/bio.20121370 [PubMed: 23213483]

Kovar DR, Harris ES, Mahaffy R, Higgs HN, & Pollard TD (2006). Control of the assembly of ATP- and ADP-actin by formins and profilin. Cell, 124, 423–435. 10.1016/j.cell.2005.11.038 [PubMed: 16439214]

Kovar DR, & Pollard TD (2004). Insertional assembly of actin filament barbed ends in association with formins produces piconewton forces. Proceedings of the National Academy of Sciences of the United States of America, 101, 14725–14730. 10.1073/pnas.0405902101 [PubMed: 15377785]

Lecroisey C, Ségalat L, & Gieseler K (2007). The *C. elegans* dense body: anchoring and signaling structure of the muscle. Journal of Muscle Research and Cell Motility, 28, 79–87. 10.1007/s10974-007-9104-y [PubMed: 17492481]

Mangio RS, Votra S, & Pruyne D (2015). The canonical eIF4E isoform of *C. elegans* regulates growth, embryogenesis, and germline sex-determination. Biology Open, 4, 843–851. 10.1242/bio.011585 [PubMed: 25979704]

Mello CC, Kramer JM, Stinchcomb D, & Ambros V (1991). Efficient gene transfer in *C.elegans*: extrachromosomal maintenance and integration of transforming sequences. The EMBO Journal, 10, 3959–3970. [PubMed: 1935914]

Mi-Mi L, & Pruyne D (2015). Loss of Sarcomere-associated Formins Disrupts Z-line Organization, but does not Prevent Thin Filament Assembly in *Caenorhabditis elegans* Muscle. Journal of Cytology & Histology, 6, 318 10.4172/2157-7099.1000318 [PubMed: 26161293]

Mi-Mi L, Votra S, Kemphues K, Bretscher A, & Pruyne D (2012). Z-line formins promote contractile lattice growth and maintenance in striated muscles of *C. elegans*. Journal of Cell Biology, 198, 87–102. 10.1083/jcb.201202053

Moerman D, & Williams BD (2006). Sarcomere assembly in *C. elegans* muscle WormBook, ed. The *C. elegans* Research Community, Wormbook 10.1895/wormbook.1.81.1

Molnár I, Migh E, Szikora S, Kalmár T, Végh AG, Deák F, Barkó S, Bugyi B, Orfanos Z, Kovács J, Juhász G, Váró G, Nyitrai M, Sparrow J, & Mihály J (2014). DAAM Is Required for Thin Filament Formation and Sarcomerogenesis during Muscle Development in Drosophila. PLoS Genetics, 10, e1004166 10.1371/journal.pgen.1004166 [PubMed: 24586196]

Moseley JB, Sagot I, Manning AL, Xu Y, Eck MJ, Pellman D, & Goode BL (2004). A Conserved Mechanism for Bni1- and mDia1-induced Actin Assembly and Dual Regulation of Bni1 by Bud6 and Profilin. Molecular Biology of the Cell, 15, 896–907. 10.1091/mbc.E03-08-0621 [PubMed: 14657240]

Ochoa JP, Sabater-Molina M, García-Pinilla JM, Mogensen J, Restrepo-Córdoba A, Palomino-Doza J, Villacorta E, Martinez-Moreno M, Ramos-Maqueda J, Zorio E, Peña-Peña ML, García-Granja PE, Rodríguez-Palomares JF, Cárdenas-Reyes IJ, de la Torre-Carpente MM, et al. (2018). Formin Homology 2 Domain Containing 3 (FHOD3) Is a Genetic Basis for Hypertrophic Cardiomyopathy. Journal of the American College of Cardiology, 72, 2457–2467. 10.1016/j.jacc.2018.10.001 [PubMed: 30442288]

Pavelec DM, Lachowiec J, Duchaine TF, Smith HE, & Kennedy S (2009). Requirement for the ERI/DICER complex in endogenous RNA interference and sperm development in *Caenorhabditis elegans*. Genetics, 183, 1283–1295. 10.1534/genetics.109.108134 [PubMed: 19797044]

Pring M, Evangelista M, Boone C, Yang C, & Zigmond SH (2003). Mechanism of Formin-Induced Nucleation of Actin Filaments. Biochemistry, 42, 486–496. 10.1021/bi026520j [PubMed: 12525176]

Pruyne D (2016). Revisiting the Phylogeny of the Animal Formins: Two New Subtypes, Relationships with Multiple Wing Hairs Proteins, and a Lost Human Formin. PloS One, 11, e0164067 10.1371/journal.pone.0164067 [PubMed: 27695129]

Pruyne D, Evangelista M, Yang C, Bi E, Zigmond S, Bretscher A, & Boone C (2002). Role of formins in actin assembly: nucleation and barbed-end association. Science, 297, 612–615. 10.1126/science.1072309 [PubMed: 12052901]

Refai O, Smit RB, Votra S, Pruyne D, & Mains PE (2018). Tissue-specific functions of *fem-2*/PP2c phosphotase and *fhod-1*/formin during *Caenorhabditis elegans* embryonic morphogenesis. G3: GENES GENOMES GENETICS, 8, 2277–2290. 10.1534/g3.118.200274 [PubMed: 29720391]

Romero S, Le Clainche C, Didry D, Egile C, Pantaloni D, & Carlier MF (2004). Formin is a processive motor that requires profilin to accelerate actin assembly and associated ATP hydrolysis. Cell, 119, 419–429. 10.1016/j.cell.2004.09.039 [PubMed: 15507212]

Rosado M, Barber CF, Berciu C, Feldman S, Birren SJ, Nicastro D, & Goode BL (2014). Critical roles for multiple formins during cardiac myofibril development and repair. Molecular Biology of the Cell, 25, 811–827. 10.1091/mbc.E13-08-0443 [PubMed: 24430873]

Sagot I, Rodal AA, Moseley J, Goode BL, & Pellman D (2002). An actin nucleation mechanism mediated by Bni1 and profilin. Nature Cell Biology, 4, 626–631. 10.1038/ncb834 [PubMed: 12134165]

Sanger JW, Wang J, Fan Y, White J, Mi-Mi L, Dube DK, Sanger JM, & Pruyne D (2017). Assembly and Maintenance of Myofibrils in Striated Muscle. Handbook of Experimental Pharmacology, 235, 39–75. 10.1007/164_2016_53 [PubMed: 27832381]

Schneider CA, Rasband WS, & Eliceiri KW (2012). NIH Image to ImageJ: 25 years of image analysis. Nature Methods, 9, 671–675. 10.1038/nmeth.2089 [PubMed: 22930834]

Severson AF, Baillie DL, & Bowerman B (2002). A formin homology protein and a profilin are required for cytokinesis and Arp2/3-independent assembly of cortical microfilaments in *C. elegans*. Current Biology, 12, 2066–2075. 10.1016/s0960-9822(02)01355-6 [PubMed: 12498681]

Shaye DD, & Greenwald I (2016). A network of conserved formins, regulated by the guanine exchange factor EXC-5 and the GTPase CDC-42, modulates tubulogenesis in vivo. Development, 143, 4173–4181. 10.1242/dev.141861 [PubMed: 27697907]

Shwartz A, Dhanyasi N, Schejter ED, & Shilo B-Z (2016). The *Drosophila* formin Fhos is a primary mediator of sarcomeric thin-filament array assembly. ELife, 5, e16540 10.7554/eLife.16540 [PubMed: 27731794]

Sikorski RS, & Hieter P (1989). A system of shuttle vectors and yeast host strains designed for efficient manipulation of DNA in *Saccharomyces cerevisiae*. Genetics, 122, 19–27. [PubMed: 2659436]

Swan KA, Severson AF, Carter JC, Martin PR, Schnabel H, Schnabel R, & Bowerman B (1998). *cyk-1*: a *C. elegans* FH gene required for a late step in embryonic cytokinesis. Journal of Cell Science, 111, 2017–2027. [PubMed: 9645949]

Takano K, Watanabe-Takano H, Suetsugu S, Kurita S, Tsujita K, Kimura S, Karatsu T, Takenawa T, & Endo T (2010). Nebulin and N-WASP Cooperate to Cause IGF-1–Induced Sarcomeric Actin Filament Formation. Science, 330, 1536–1540. 10.1126/science.1197767 [PubMed: 21148390]

Taniguchi K, Takeya R, Suetsugu S, Kan-O M, Narusawa M, Shiose A, Tominaga R, & Sumimoto H (2009). Mammalian formin fhod3 regulates actin assembly and sarcomere organization in striated muscles. Journal of Biological Chemistry, 284, 29873–29881. 10.1074/jbc.M109.059303

Timmons L, & Fire A (1998). Specific interference by ingested dsRNA. Nature, 395, 854 10.1038/27579. [PubMed: 9804418]

Ushijima T, Fujimoto N, Matsuyama S, Kan-O M, Kiyonari H, Shioi G, Kage Y, Yamasaki S, Takeya R, & Sumimoto H (2018). The actin-organizing formin protein Fhod3 is required for postnatal development and functional maintenance of the adult heart in mice. Journal of Biological Chemistry, 293, 148–162. 10.1074/jbc.M117.813931

Vanneste CA, Pruyne D, & Mains PE (2013). The role of the formin gene *fhod-1* in *C. elegans* embryonic morphogenesis. Worm, 2, e25040 10.4161/worm.25040 [PubMed: 24778933]

Wang J, & Barr MM (2005). RNA interference in *Caenorhabditis elegans*. Methods in Enzymology, 392, 36–55. 10.1016/S0076-6879(04)92003-4 [PubMed: 15644174]

Wooten EC, Hebl VB, Wolf MJ, Greytak SR, Orr NM, Draper I, Calvino JE, Kapur NK, Maron MS, Kullo IJ, Ommen SR, Bos JM, Ackerman MJ & Huggins GS (2013). Formin Homology 2 Domain Containing 3 Variants Associated with Hypertrophic Cardiomyopathy. Circulation: Cardiovascular Genetics, 46, 10–18. 10.1161/CIRCGENETICS.112.965277

Yuen M, Sandaradura SA, Dowling JJ, Kostyukova AS, Moroz N, Quinlan KG, et al. (2014). Leiomodin-3 dysfunction results in thin filament disorganization and nemaline myopathy. The Journal of Clinical Investigation, 124, 4693–4708. 10.1172/JCI75199 [PubMed: 25250574]
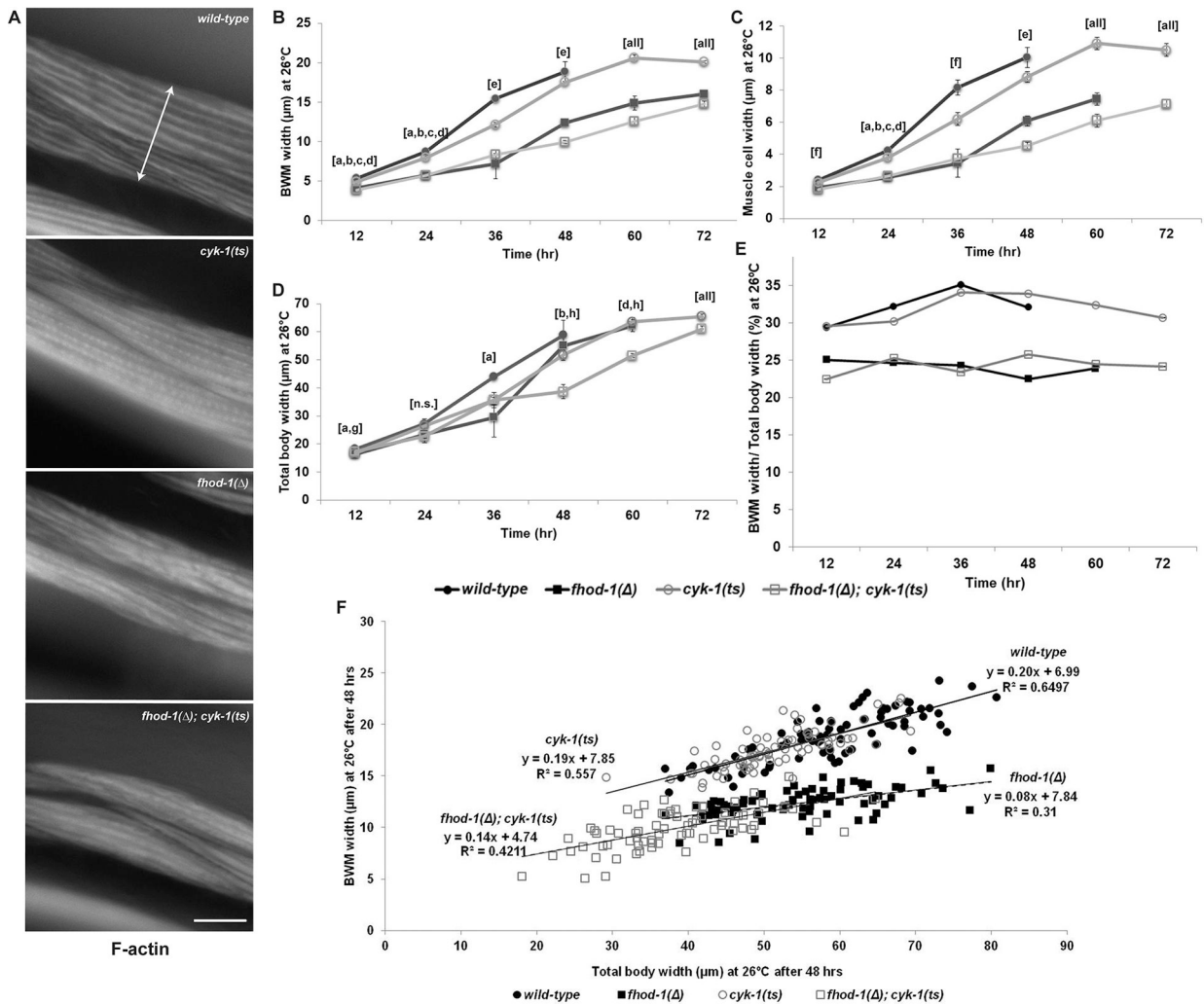
Figure 1. Post-embryonic CYK-1 loss causes minimal BWM defects.

Larvae hatched at permissive temperature (16°C) were grown at restrictive temperature (26°C) for up to 72 hrs before staining with fluorescently-labeled phalloidin to show F-actin. (A) Dorsal views of BWM in worms of indicated genotypes grown 60 hrs. Double arrow shows lateral width of one BWM. Scale bar, 20 μm. (B) BWM widths, (C) individual muscle cell widths, and (D) total body widths were measured. Graphs depict average of the means of three experiments (n = 25 animals per strain per experiment, one body, two BWMs, and four muscle cells per animal). Error bars indicate standard error of the mean (SEM). Statistical significance p < 0.05 is indicated for: (a) wild type vs *fhod-1(   )*; (b) wild type vs double mutant; (c) *cyk-1(ts)* vs *fhod-1(   )*; (d) *cyk-1(ts)* vs double mutant; (e) all comparisons except wild type vs *cyk-1(ts)*; (f) all comparisons except *fhod-1(   )* vs double mutant; (g) wild type vs *cyk-1(ts)*; (h) *fhod-1(   )* vs double mutant; (all) all comparisons; or (n.s.) differences were not significant for any comparison, p   0.05. (E) Calculated ratio of (B) average BWM width to (D) average total body width. (F) Plot of BWM width versus total body width for 75 individual worms of each genotype grown at restrictive temperature 48 hrs, with linear trendlines shown. Wild-type and *cyk-1(ts)* animals show nearly identical linear relationships between total body and BWM width, suggesting the smaller BWM size

of *cyk-1(ts)* animals may be a secondary consequence of smaller body size. Approximately linear relationships between BWM and total body sizes for *fhod-1( )* and *fhod-1( );* *cyk-1(ts)* animals were similar to each other, but with smaller muscle-to-body ratios than wild type.
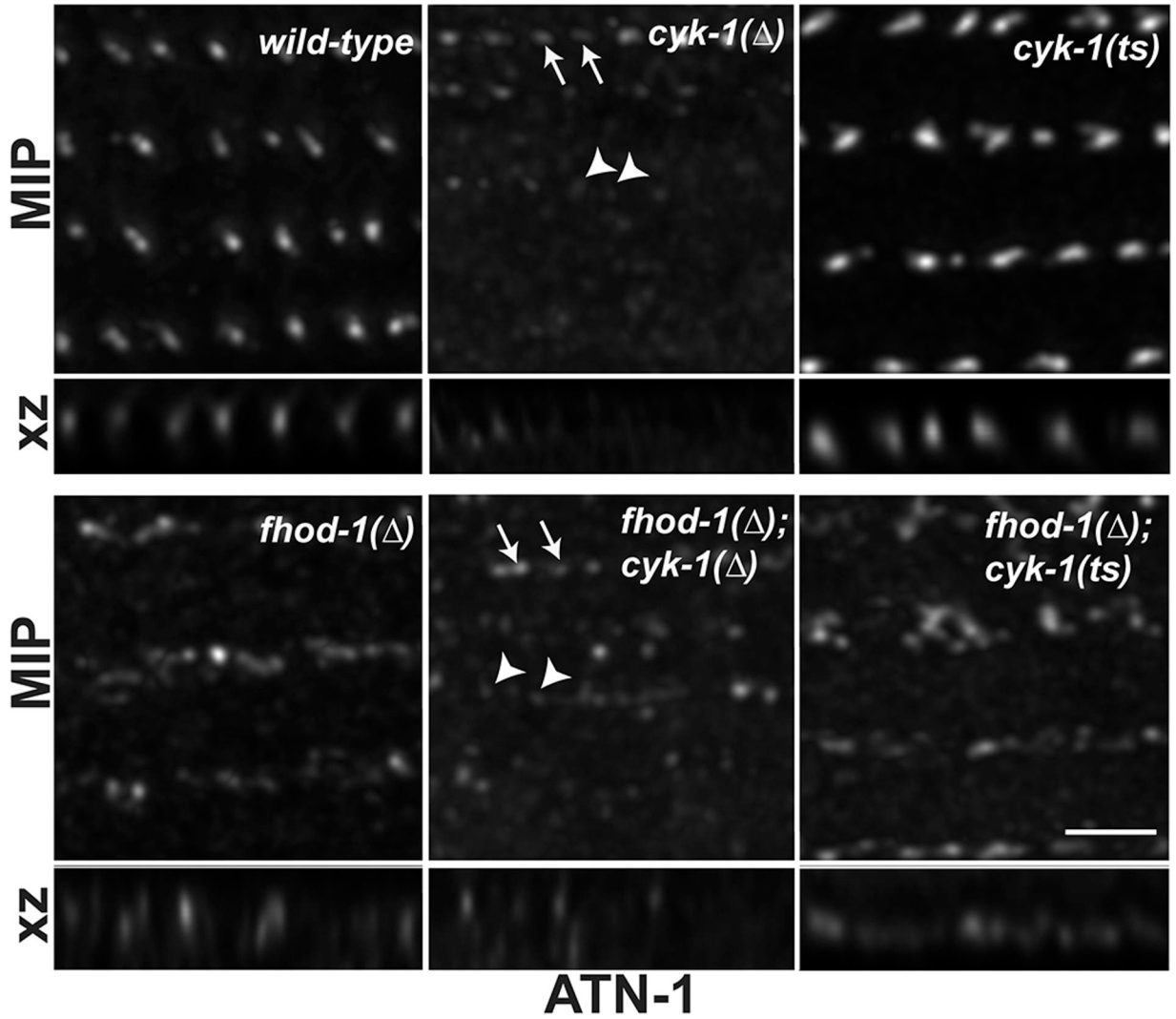
Figure 2. Constitutive absence of FHOD-1 or CYK-1, but not post-embryonic loss of CYK-1, disrupts DB organization.

Maximum intensity projections (MIP) of dorsal views and reconstructed side views (XZ projection) of DBs in age-synchronized adult worms after ATN-1 immunostain. Scale bar, 2 μm. DBs appear as discrete puncta in wild-type BWM and partially dispersed in *fhod-1( )* mutants. DBs of *cyk-1( )* and *fhod-1( ); cyk-1( )* mutants possess areas of stronger stain (arrows) and extremely faint stain (arrowheads). DBs of *cyk-1(ts)* appear as puncta, and those of *fhod-1( ); cyk-1(ts)* mutants appear partially dispersed.
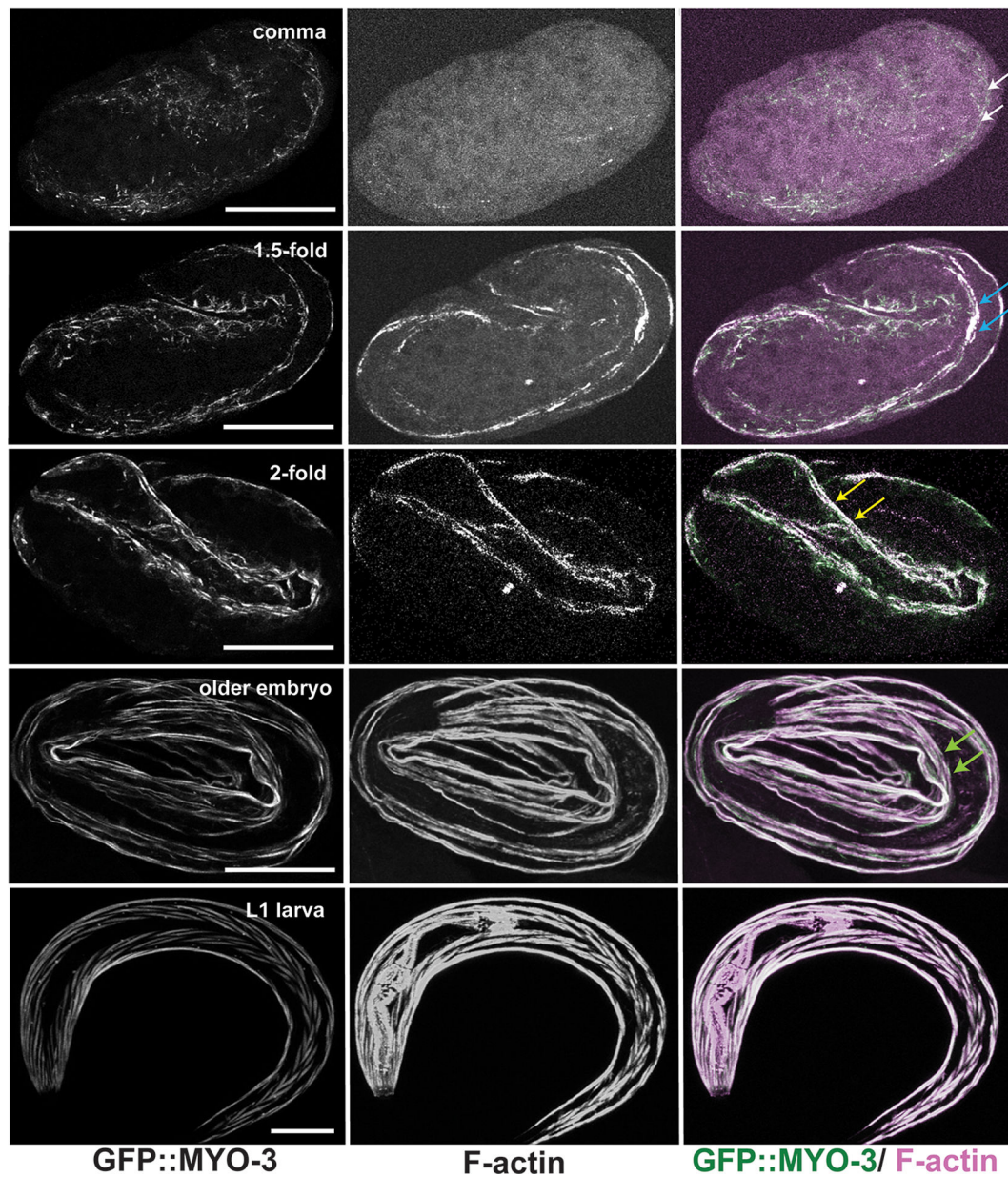
Figure 3. Development of the myofilament lattice in wild-type embryonic BWM.
Maximum intensity projections (MIP) of embryos expressing GFP::MYO-3 (a BWM marker) and stained for F-actin, show BWM development at embryonic stages comma, 1.5-fold, 2-fold, older than 2-fold, and L1 larva. At comma stage, traces of F-actin appear as polarization of muscle components begins (white arrows). Polarization continues through the 1.5-fold stage, where F-actin and GFP::MYO-3 strongly accumulate (blue arrows). The first sarcomeres form just prior to the 2-fold stage with appearance of defined striations (yellow arrows). Stages older than 2-fold (older embryo, L1 larva) feature neatly aligned striations (green arrows) in BWM. Scale bars, 20 μm.
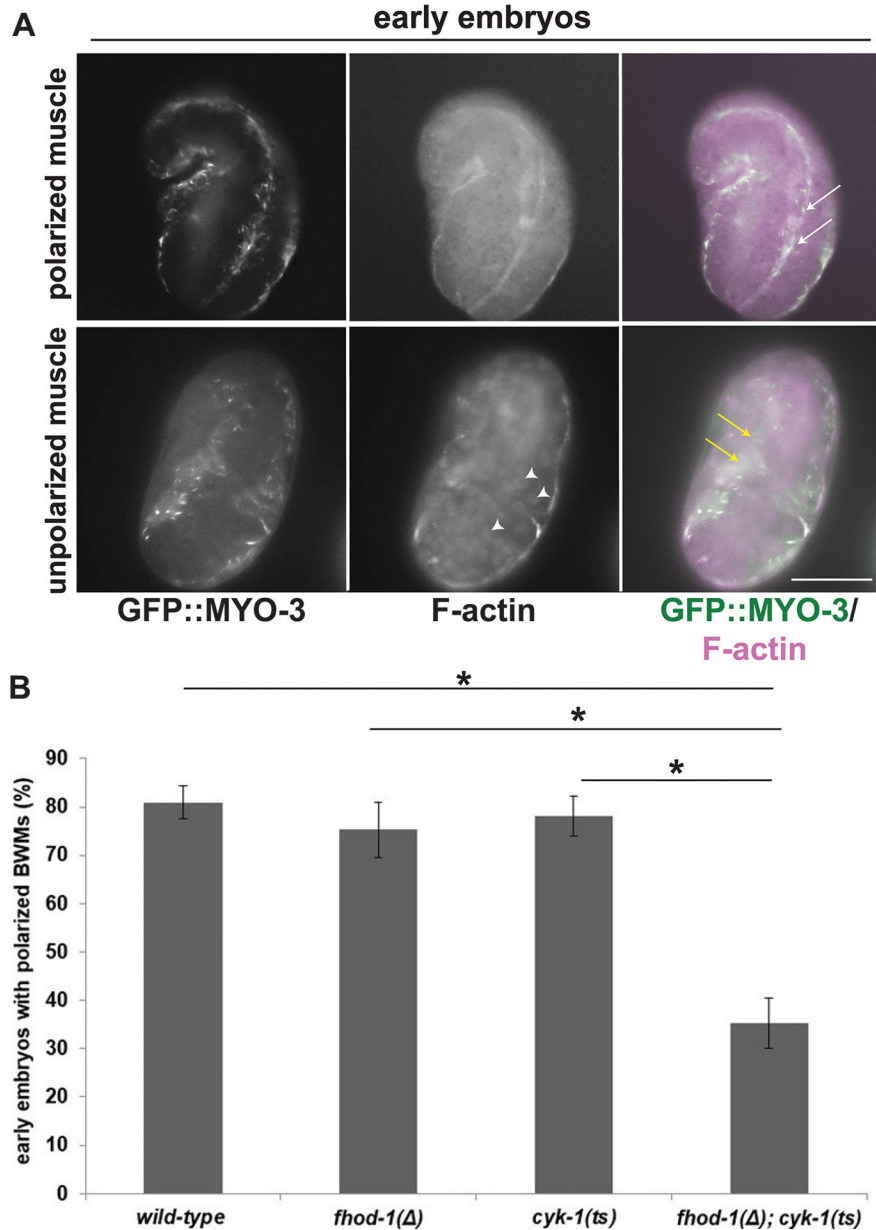
Figure 4. Simultaneous absence of FHOD-1 and CYK-1 delays polarization of sarcomere components in early embryonic BWMs.

GFP-myosin-expressing embryos grown at permissive temperature were shifted to restrictive temperature 30 min before staining for F-actin. (A) Polarization of sarcomere components (white arrows) is normally observable in early embryos (comma to 1.5-fold stage), although not always (white arrows). Scale bar, 20 µm. (B) Quantification shows BWM in a majority of wild-type and single formin mutant embryos polarizes (normal), while polarization has not yet occurred in a majority of *fhod-1( ); cyk-1(ts)* double mutants. Data are averages of the means of three experiments ± SEM (n = 35 early or 70 late embryos, per strain per experiment). (*) indicates p < 0.01. Differences in all other pairwise comparisons were not statistically significant (p > 0.05). Also visible in (A), F-actin accumulates in nuclei (arrowheads) of embryos bearing *cyk-1(ts)* (see Figure S4).
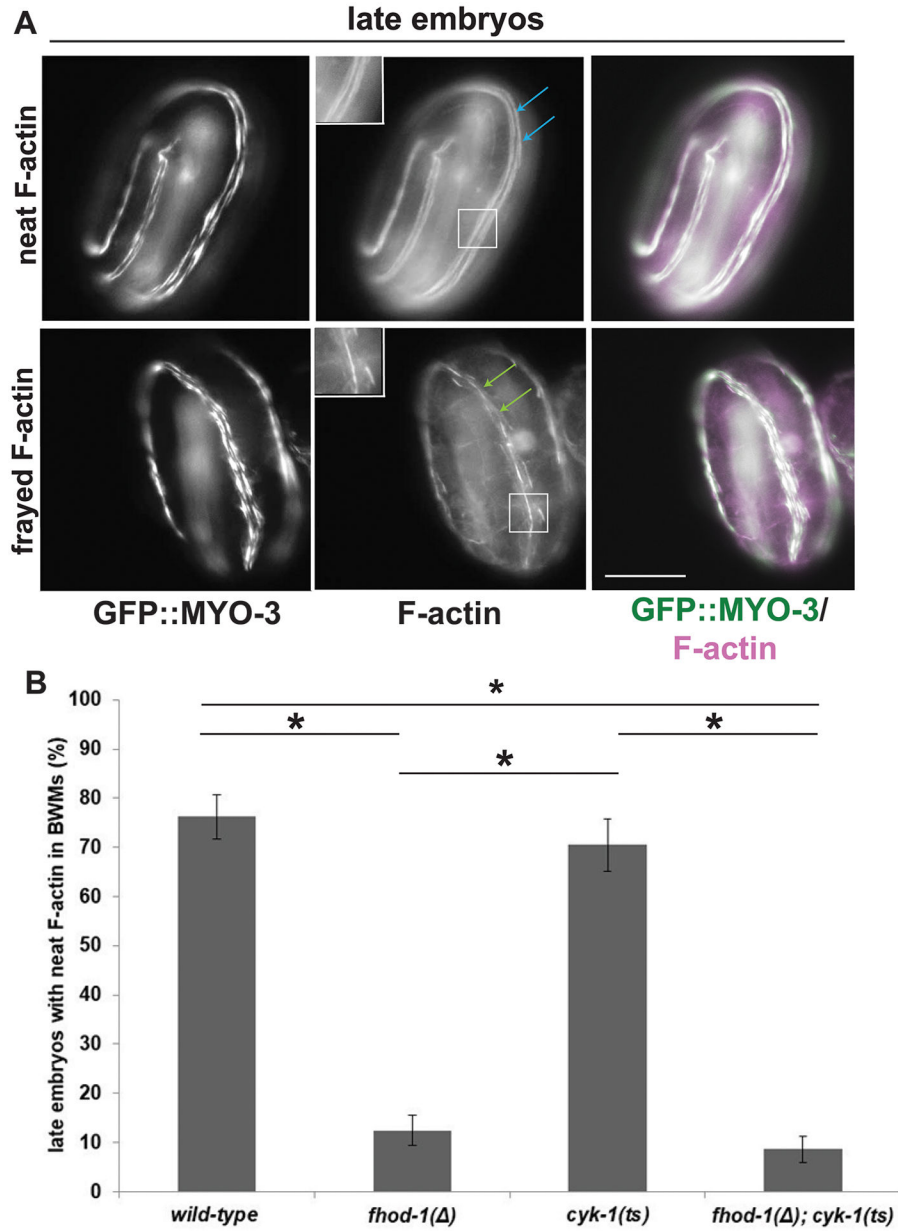
Figure 5. Absence of FHOD-1 causes frayed F-actin striations in late embryonic BWM.
(A) In later stage embryos (2-fold and older) grown at permissive temperature and shifted to restrictive temperature for 30 min, fluorescent phalloidin stain typically reveals neat F-actin-rich striations (blue arrows), but striations appear frayed (green arrows) in a subset of embryos. Scale bar, 20 μm. Insets show higher magnification of boxed areas. (B) Quantification shows higher frequency of frayed striations (and lower frequency of neat-appearing striations) correlates with *fhod-1( )*, irrespective of *cyk-1*. Data are averages of the means of three experiments ± SEM (n = 35 early or 70 late embryos, per strain per experiment). (*) indicates p < 0.01. Differences in all other pairwise comparisons were not statistically significant (p > 0.05).
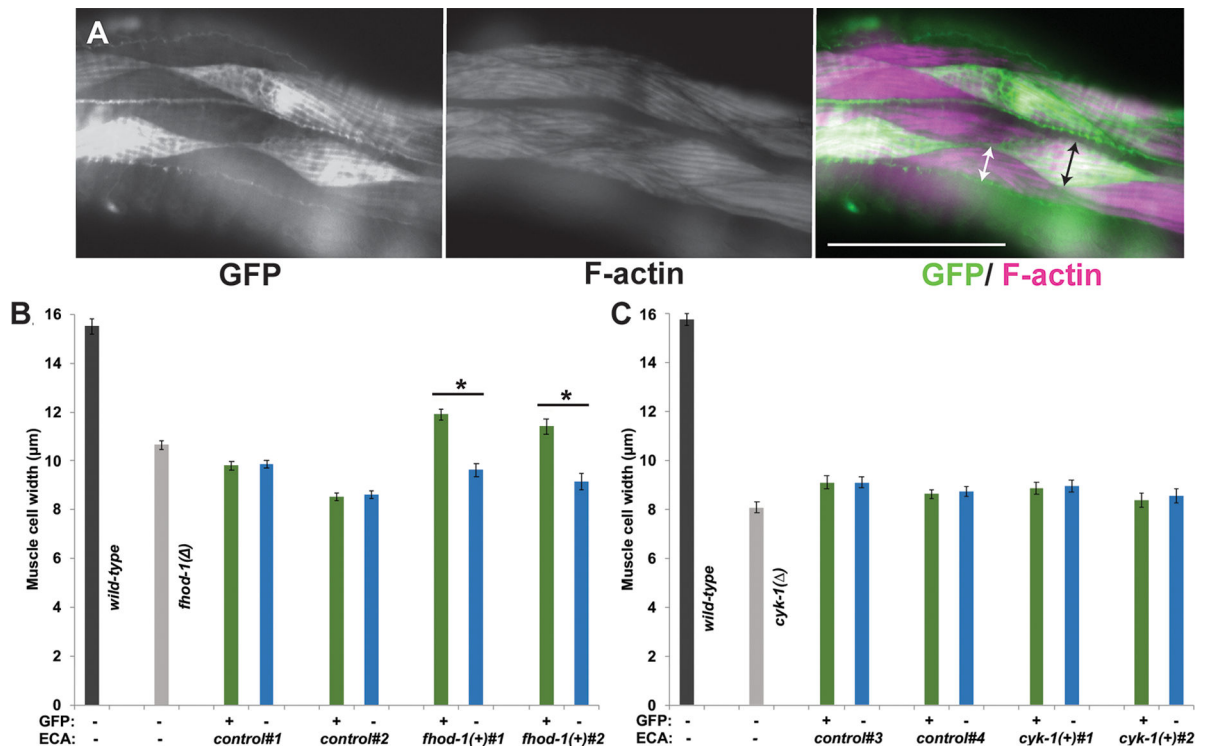
Figure 6. FHOD-1 plays a muscle cell autonomous role in promoting BWM cell growth whereas CYK-1 does not.

Homozygous *fhod-1( )* or heterozygous *cyk-1( )/+* transgenic lines were selected for mosaic inheritance of extrachromosomal arrays (ECAs) containing wild-type *fhod-1* or *cyk-1*, respectively, along with a muscle-expressed *gfp* gene. Similar control transgenic lines were selected for mosaic inheritance of ECAs constructed from non-formin DNA and the GFP marker. Two independently isolated lines of each genotype were selected, together with non-transformed wild-type and mutant controls, for analysis. (A) Fluorescent phalloidin stain of a worm with mosaic GFP expression allows comparison of cell widths of transgenic GFP-positive BWM cells (black arrow) and adjacent non-transgenic GFP-negative BWM cells (white arrow). Scale bar, 50 μm. (B) For *fhod-1( )* adults bearing ECAs *control#1* and *control#2* without *fhod-1(+),* there was no significant effect of ECA presence on muscle cell size. Conversely, for *fhod-1( )* adults bearing ECAs *fhod-1(+)#1* and *fhod-1(+)#2* with *fhod-1(+),* transgenic BWM cells (green bars) were significantly wider than non-transgenic cells in the same animal (blue bars). (C) For analysis of *cyk-1*, ECA-bearing homozygous *cyk-1( )* adult progeny of *cyk-1( )/+* parents were examined. ECAs *cyk-1(+)#1* and *cyk-1(+)#2* with *cyk-1(+)* had no significant effect on widths of transgenic BWM cells (green bars) compared to non-transgenic cells (blue bars), and were similar in size to those in non-transformed *cyk-1( )* adults. Graphs show averages ± SEM (n = 30 worms for each genotype, harvested and stained over three independent sessions for (B) *fhod-1* mosaic analysis, or seven independent sessions for (C) *cyk-1* mosaic analysis). (*) indicates $p < 0.01$. Differences in all other pairwise comparisons were not statistically significant ($p > 0.05$).
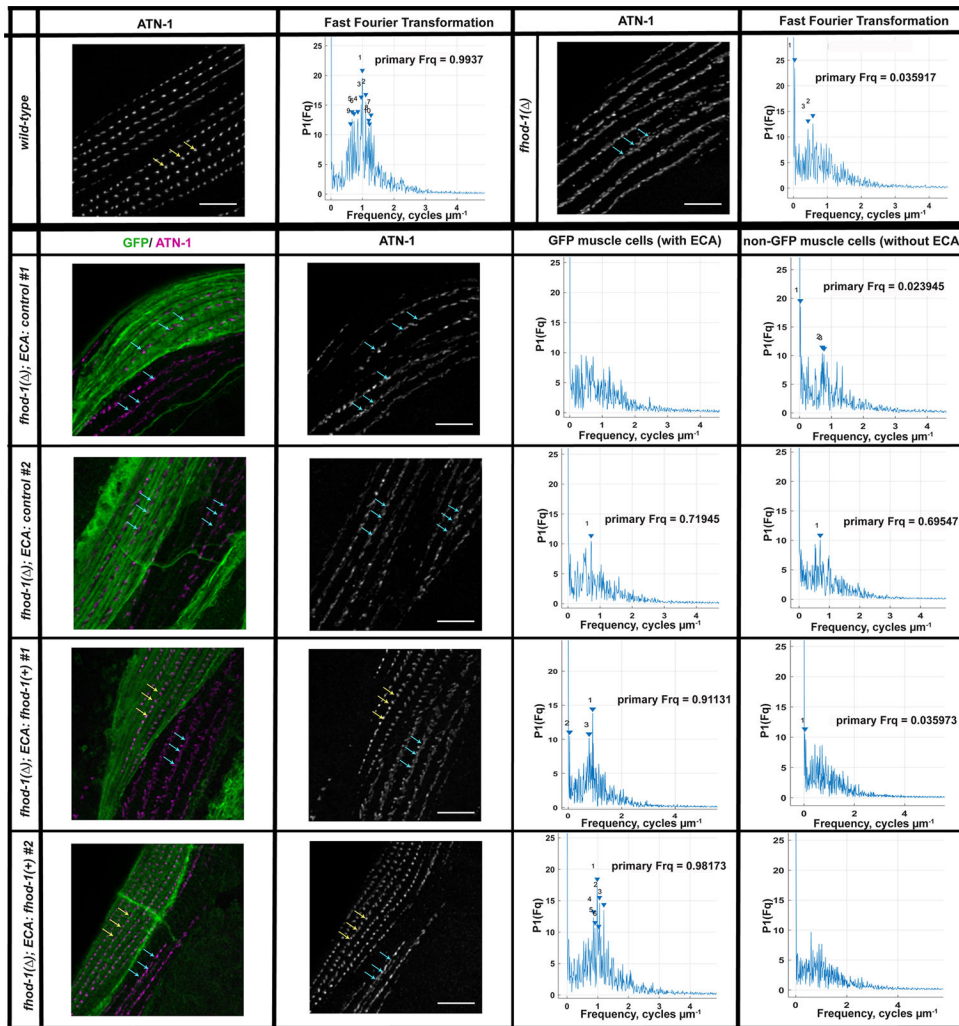
Figure 7. FHOD-1 promotes proper DB morphology in a cell autonomous manner.
Wild-type, non-transformed *fhod-1( )*, and *fhod-1( )* worms with mosaic inheritance of ECAs (from Figure 6) were immunostained for ATN-1 and GFP. As shown in maximum intensity projections (MIP) of dorsal views from age-synchronized adults, ATN-1-positive DBs are punctate and regularly spaced in wild-type BWM, or *fhod-1( )* BWM cells that inherit a *fhod-1(+)*-containing ECA (yellow arrows), whereas DBs appear partially dispersed and irregular in *fhod-1( )* BWM cells that inherit either no ECA or an ECA lacking *fhod-1(+)* (blue arrows). DB spacing was analyzed by performing fast Fourier transform (FFT) on concatenated intensity profiles of ATN-1 immunostain along approximately eight striations within single BWM cells (n = 10 animals per strain, one ECA-containing BWM cell and one BWM cell lacking an ECA per animal for transgenic lines; one BWM cell for non-transformed animals). Amplitude spectra for wild-type cells or *fhod-1( )* cells that inherited a *fhod-1(+)*-containing ECA show clustering of peaks 0.8–1.0 μm^{-1}, while spectra peaks did not cluster near any particular frequency for *fhod-1( )* cells that inherited no ECA or an ECA lacking *fhod-1(+)*. Scale bars, 5 μm. Similar results were obtained for two additional replicate experiments (Figure S6).
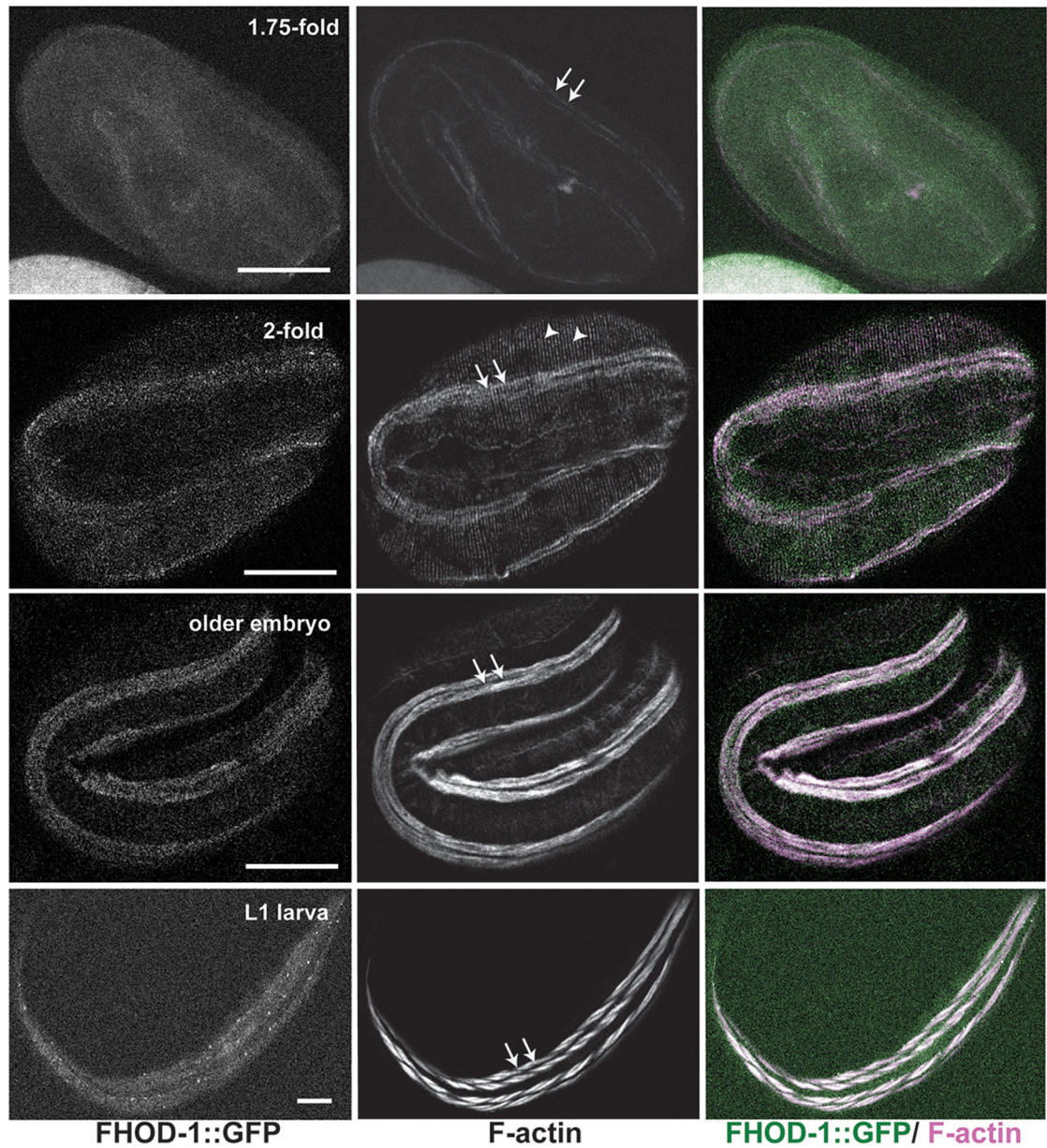
Figure 8. Distribution of FHOD-1::GFP in developing BWM.
FHOD-1::GFP-expressing embryos and larvae of indicated stages were stained to visualize F-actin. FHOD-1::GFP localizes diffusely in early (1.75-fold) embryonic BWM, with gradual development of a punctuate appearance that becomes prominent in larval (L1) BWM. Note, in addition to staining F-actin striations in muscle (arrows), phalloidin decorates F-actin bundles in the epidermis (arrowheads). Scale bars, 20 μm.
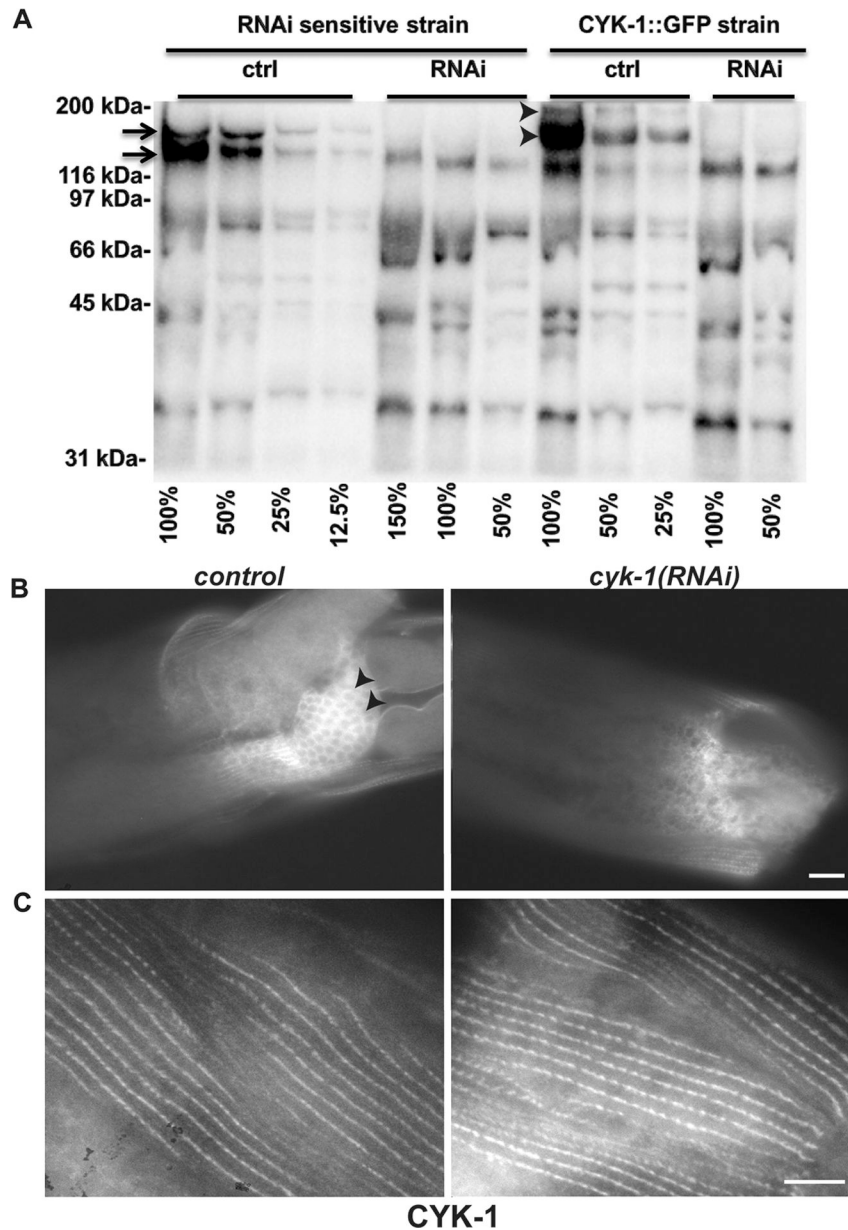
Figure 9. *cyk-1(RNAi)* does not alter DB-associated CYK-1 immunostain.

(A) Western blot for CYK-1 on dilutions (expressed as percentages) of extracts from adult animals treated for control or *cyk-1(RNAi)*. Sample loads were approximately normalized based on previous whole lane protein determined by Coomassie Brilliant Blue staining. In RNAi-sensitive *cyk-1(+)* animals, bands at approximately 160 kDa and 170 kDa (arrows) for CYK-1 were lost after *cyk-1(RNAi)* but not control RNAi for 5 days, as were bands of approximately 187 kDa and 197 kDa (arrowheads) for CYK-1::GFP from animals in which endogenous *cyk-1* was tagged with *gfp*. Unaffected bands recognized by this polyclonal anti-CYK-1 were presumed non-specific. (B) CYK-1 immunostain decorates the germline in control animals (arrowheads) but not after *cyk-1(RNAi)*, whereas (C) anti-CYK-1 stain of

DBs is similar between control and *cyk-1(RNAi)* animals, suggesting DB-associated stain is non-specific. Scale bars, 10 μm.

Table 1.

Worm strains used in this study.

Strain names, genotypes, figure(s) in which they appear, and source.

Strain	Genotype	Source *†*	Figure(s)
DWP008	*cyk-1(ok2300)/+ III*	Mi-Mi et al., 2012	
DWP009	*fhod-1(tm2363) I; cyk-1(ok2300)/+ III*	Mi-Mi et al., 2012	
DWP010	*fhod-1(tm2363) I; qaIs8001[fhod-1::gfp mini-unc-119(+)]*	Mi-Mi et al., 2012	8, S7
DWP022	*cyk-1(ok2300) unc-119(ed4?)/cyk-1(ok2300) + III; upsIs3[cyk-1::gfp mini-unc-119(+)]*	Mi-Mi et al., 2012	S5
DWP028	*eri-1(mg366) IV; rhIs2[pat-3::HA::gfp]*	Mi-Mi et al., 2012	9
DWP068	*fhod-1(tm2363) I; cyk-1(or596ts) III*	XA8001 × JCC389	1,2,S1
DWP153	*mT1/+ II; cyk-1(ok2300)/mT1[dpy-10(e128)] III*	DWP008 × mT1/+	2,6,S5
DWP154	*fhod-1(tm2363) I; mT1/+ II; cyk-1(ok2300)/ mT1[dpy-10(e128)] III*	DWP009 × mT1/+	2
DWP156	*fhod-1(tm2363) I; stEx30[myo-3p::gfp::myo-3 rol-6(su1006gf)]*	XA8001 × RW1596	4,5,S3
DWP160	*cyk-1(or596ts) III; stEx30[myo-3p::gfp::myo-3 rol-6(su1006gf)]*	JCC389 × RW1596	4,5,S3,S4
DWP161	*fhod-1(tm2363) I; cyk-1(or596) III; stEx30[myo-3p::gfp::myo-3 rol-6(su1006gf)]*	DWP068 × RW1596	4,5,S3,S4
DWP199	*fhod-1(tm2363) I; upsEx136[fhod-1(+) myo-2p::gfp myo-3p::gfp rab-3p::gfp]*	XA8001	6,7,S6
DWP202	*fhod-1(tm2363) I; upsEx139[fhod-1(+) myo-2p::gfp myo-3p::gfp rab-3p::gfp]*	XA8001	6,7,S6
DWP204	*fhod-1(tm2363) I; upsEx141[myo-2p::gfp myo-3p::gfp rab-3p::gfp]*	XA8001	6,7,S6
DWP206	*fhod-1(tm2363) I; upsEx143[myo-2p::gfp myo-3p::gfp rab-3p::gfp]*	XA8001	6,7,S6
DWP208	*+/mT1 II; cyk-1(ok2300)/mT1[dpy-10(e128)] III; upsEx145[cyk-1(+) myo-2p::gfp myo-3p::gfp rab-3p::gfp]*	DWP153	6
DWP209	*+/mT1 II; cyk-1(ok2300)/mT1[dpy-10(e128)] III; upsEx146[cyk-1(+) myo-2p::gfp myo-3p::gfp rab-3p::gfp]*	DWP153	6
DWP211	*+/mT1 II; cyk-1(ok2300)/mT1[dpy-10(e128)] III; upsEx148[myo-2p::gfp myo-3p::gfp rab-3p::gfp]*	DWP153	6
DWP213	*+/mT1 II; cyk-1(ok2300)/mT1[dpy-10(e128)] III; upsEx150[myo-2p::gfp myo-3p::gfp rab-3p::gfp]*	DWP153	6
DWP219	*daam-1(ups39) V*	This study	S2
DWP222	*fhod-1(tm2363) I; daam-1(ups39) V*	DWP219 × XA8001	S2
GS7933	*unc-119(ed3) pha-1(e2123ts) III; arIs195[exc::LifeAct::gfp unc-119(+)]; arEx2357[cyk-1::gfp hygrR(pIR98) pha-1(+)(pBS)*	Shaye & Greenwald, 2016	S8
JCC389	*cyk-1(or596ts) III*	Davies et al., 2014	1,2,S1
JCC955	*cyk-1(jcc4[cyk-1::gfp::3xflag]) III*	Davies et al., 2018	9,S8
N2	Bristol wild type	CGC *‡*	1,2,6,7,S1,S2, S5,S6,S7
RW1596	*myo-3(st386) V; stEx30[myo-3p::gfp::myo-3 rol-6(su1006gf)]*	Campagnola et al., 2002	3,4,5,S3,S4
XA8001	*fhod-1(tm2363) I*	Mi-Mi et al., 2012	1,2,6,7,S1,S2,S6

† Reference for initial isolation, or parental strains for crossing or transgenesis in this study.

‡ Caenorhabditis Genetic Center (University of Minnesota, Minneapolis, MN)